UR-1561
FERMILAB-PUB-99-024-E

Precision Calibration of the NuTeV Calorimeter

D. A. HARRIS[7], J. YU[3], T. ADAMS[4], A. ALTON[4], S. AVVAKUMOV[7], L. de BARBARO[5], P. de BARBARO[7], R. H. BERNSTEIN[3], A. BODEK[7], T. BOLTON[4], J. BRAU[6], D. BUCHHOLZ[5], H. BUDD[7], L. BUGEL[3], J. CONRAD[2], R. B. DRUCKER[6], J. FORMAGGIO[2], R. FREY[6], J. GOLDMAN[4], M. GONCHAROV[4], R. A. JOHNSON[1], J. H. KIM[2], S. KOUTSOLIOTAS[2], G. KRISHNASWAMI[7], M. J. LAMM[3], W. MARSH[3], D. MASON[6], C. McNULTY[2], K. S. McFARLAND[3,7], D. NAPLES[4], P. NIENABER[3], A. ROMOSAN[2], W. K. SAKUMOTO[7], H. SCHELLMAN[5], M. H. SHAEVITZ[2], P. SPENTZOURIS[2,3], E. G. STERN[2], B. TAMMINGA[2], A. VAITAITIS[2], M. VAKILI[1], E. VAN ARK[7,5], V. WU[1], U. K. YANG[7], and G. P. ZELLER[5]

(The NuTeV Collaboration)

[1] *University of Cincinnati, Cincinnati, OH 45221*
[2] *Columbia University, New York, NY 10027*
[3] *Fermi National Accelerator Laboratory, Batavia, IL 60510*
[4] *Kansas State University, Manhattan, KS 66506*
[5] *Northwestern University, Evanston, IL 60208*
[6] *University of Oregon, Eugene, OR 97403*
[7] *University of Rochester, Rochester, NY 14627*

NuTeV is a neutrino-nucleon deep-inelastic scattering experiment at Fermilab. The detector consists of an iron-scintillator sampling calorimeter interspersed with drift chambers, followed by a muon toroidal spectrometer. We present determinations of response and resolution functions of the NuTeV calorimeter for electrons, hadrons, and muons over an energy range of 4.8 to 190 GeV. The absolute hadronic energy scale is determined to an accuracy of 0.43% . We compare our measurements to predictions from calorimeter theory and GEANT3 simulations.

1 Introduction

The increased intensity of the Fermilab Tevatron fixed-target program has made it possible to qualitatively improve neutrino deep-inelastic scattering experiments. Deep-inelastic neutrino scattering probes both the electroweak and strong forces in unique ways which are both competitive and complementary to other measurements at hadron and electron colliders. For these reasons, it is important to continue improving the precision of measurements with neutrino beams. NuTeV (Fermilab Experiment 815) is designed to exploit the intensity capabilities at Fermilab using a new neutrino beam, an upgraded neutrino detector, and a continuous test beam calibration system.

The new neutrino beam uses a sign-selected, quadrupole train (SSQT) [1] to produce a high-intensity, ultra-pure beam of either neutrinos or antineutrinos. For neutrino detection, the experiment uses an upgraded version of the CCFR detector [2], shown in Figure 1, with new scintillation oil and photomultiplier tubes combined with refurbished drift chambers. In the detector, neutrino interactions produce a hadronic shower from the outgoing struck quark whose energy is measured in the target-calorimeter and, for charged current events, an associated outgoing muon whose angle (momentum) is measured in the target-calorimeter (downstream muon spectrometer).

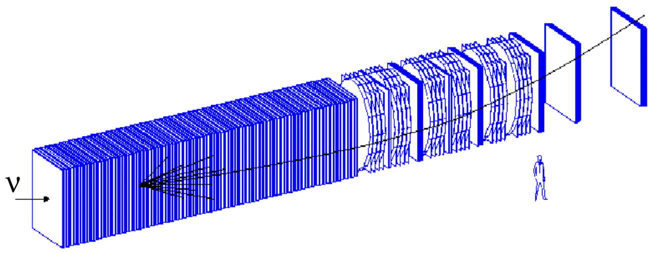

Figure 1: The NuTeV neutrino detector showing the target calorimeter followed by the downstream muon spectrometer.

The NuTeV data run took place during the Fermilab 1996-1997 fixed target run. The experiment recorded over three million neutrino and antineutrino interactions. Two of the physics goals of NuTeV are a precise measurement of the weak mixing angle and measurement of structure functions and the strong coupling constant from QCD scaling violations. Both of these results are dependent upon a detailed understanding of the response of the target-calorimeter. A previous experiment using this calorimeter, CCFR, determined the calorimeter energy scale to an uncertainty of approximately 1%. CCFR measures [3] the weak mixing angle to be $\sin^2\theta_W = 0.2236 \pm 0.0019(\text{stat}) \pm 0.0019(\text{syst}) \pm 0.0030(\text{model})$. NuTeV aims for a total precision of better than 0.002 on $\sin^2\theta_W$, primarily by changing the measurement technique to reduce model uncertainties. However, in CCFR the experimental systematic uncertainty due to calorimeter response is ± 0.0011 and the NuTeV technique is considerably more sensitive to energy calibrations. The reduced theoretical uncertainties make an improved calibration essential for the success of this measurement.

In the case of the measurement of the strong coupling constant, the systematic uncertainty on the QCD scale parameter, $\Lambda_{\overline{MS}}$, from calibration effects is at the 50-100 MeV level previously[4], which is the largest single experimental source of uncertainty in the measurement. In NuTeV, this uncertainty would be reduced by a factor of three by an absolute calibration of 0.3% uncertainty.

For the measurements listed above, the absolute response and resolution of the hadronic shower energy measurement are crucially important. For this reason, precision detector calibration and response determination is a key component of the NuTeV program. This is done using several data sets: the actual neutrino events, neutrino-induced muons from upstream shielding, and calibration beam data. Throughout the data run, the calibration beam operates continuously and provides momentum tagged electrons, muons, and hadrons with energies between 4.8 and 190 GeV. A precision spectrometer provides an event-by-event momentum determination with resolution better than 0.3% and a combination of a Čerenkov counter and a TRD are used to determine the particle type for each event.

This article describes the various techniques and studies that lead to the precision calibration of this calorimeter. First, the detector and electronics calibrations using neutrino-induced events are described, followed by the test of these techniques and resolution studies using the calibration beam data. This article also demonstrates which aspects of the detector response are accurately modeled by GEANT and other software simulation packages.

2 The NuTeV Calorimeter

The NuTeV calorimeter consists of 168 plates of steel measuring 3 m (H) $\times$ 3 m (W) $\times$ 5.1 cm (L), interspersed with 84 scintillation counters of dimension 3 m (H) $\times$ 3 m (W) $\times$ 2.5 cm (L) and 42 drift chambers. There are two plates of steel between every two consecutive scintillation counters, and one drift chamber between every other set of counters. One unit counter consists of a scintillation counter and two steel plates surrounding the scintillator. Therefore one unit calorimeter layer consists of two counters and a drift chamber. This configuration leads to a detector with 10.35 cm of steel between counters and 20.7 cm of steel between drift chambers. The geometry of one unit of the calorimeter is shown in Figure 2 and this unit is repeated 42 times to make up the entire calorimeter. Table 1 summarizes the materials and their longitudinal sizes in units of cm, radiation length, and interaction length, for one unit of the calorimeter's longitudinal layer.

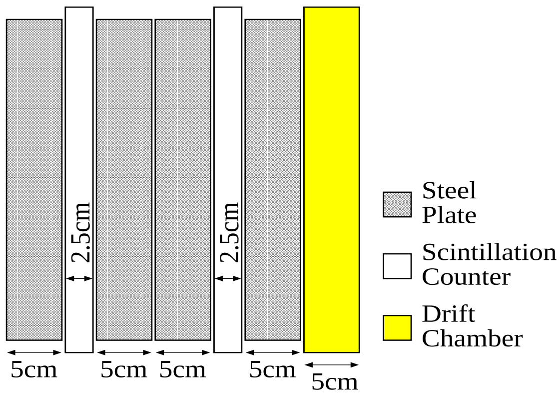

Figure 2: Geometry of one unit of the calorimeter. This unit is repeated 42 times to make up the entire calorimeter. One unit of the calorimeter consists of a scintillation counter sandwiched between two steel plates.

Figure 3 shows a schematic diagram of a NuTeV scintillation counter. The scintillation counters are lucite boxes filled with Bicron 517L scintillator oil. The counters have 3 mm vertical lucite ribs spaced by 2.5-5.1 cm, depending on the lateral position of the ribs, and designed for structural support. Since these ribs do not scintillate, the counters are staggered so that the ribs are not aligned on the transverse plane throughout the length of the calorimeter.

Each counter is surrounded by 8 wavelength-shifter bars, doped with green BBQ fluor, and is read out in four corners by photomultiplier tubes (PMT's), mounted one on each corner. The PMT's are 10-stage Hamamatsu R2154 phototubes with a green-extended photocathode, with gains set to about 10^6.

There is an air joint between the wavelength-shifter bars. The joints between the wavelength-shifter bars and the phototubes have 3 mm thick clear silicon jelly cookies for better optical and mechanical connections, as well as

Table 1: Composition in interaction length and radiation length of one unit of the NuTeV calorimeter. This unit is repeated 42 times to make up the entire calorimeter.

Component	Length		
	cm	X_0	λ_I
4 Steel Plates	20.7	11.75	1.24
2 Scint. Counters	13.0	0.51	0.16
1 Drift Chamber	3.7	0.17	0.03
Total	37.4	12.43	1.43

for PMT window protection. The cookies are made of Dow Corning Sylgard(R) 182 silicon elastomer and 182 curing agent. Given this particular geometry and readout scheme, NuTeV observes muon signal distributions which are consistent with, on average, 30 photoelectrons for muons traversing the center of a counter. For muons closer to the edge of the counter, where light collection is more efficient, the number is higher.

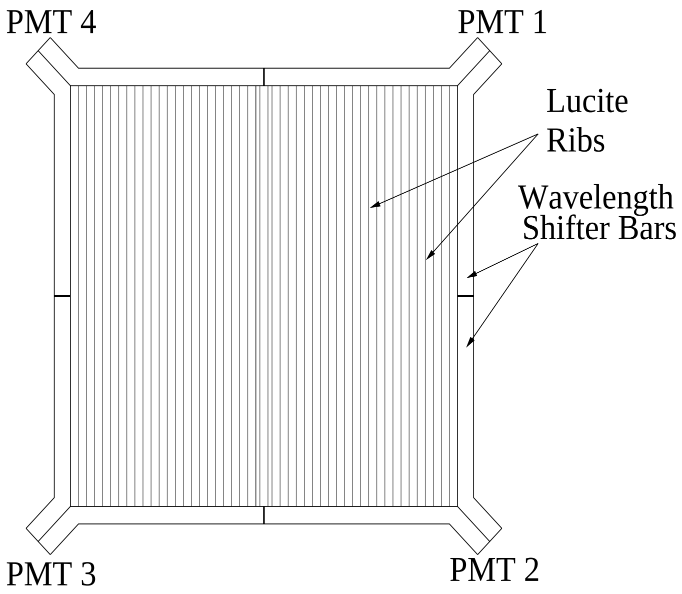

Figure 3: A schematic drawing of a NuTeV scintillation counter.

3 Calorimeter Readout Electronics

The design of the readout electronics is dictated by the requirement to accommodate a very large dynamic range of the signal using 11-bit analog-to-digital converters (ADC's). Minimum ionizing particle energy loss (MIP) in the calorimeter is approximately 0.15 GeV per unit counter while neutrino interaction induced hadronic showers could deposit up to 100 GeV into a single unit counter. Note that the actual energy deposit of a minimum ionizing particle in a single scintillation counter is approximately 4 MeV.

Figure 4 shows a schematic diagram of the readout electronics system. The readout electronic channels consist of the following three separate gains, to measure energies in a wide dynamic range:

- $HIGH$ is the signal formed by a sum of signals from each of the four PMT's of a given counter (fan-in ES-7138) [5] and $\times 10$ amplification of the summed signal by the linear amplifier LeCroy 612A. The amplified signal is then digitized by a LeCroy 4300 [6] Fast Encoding and Readout ADC (FERA).

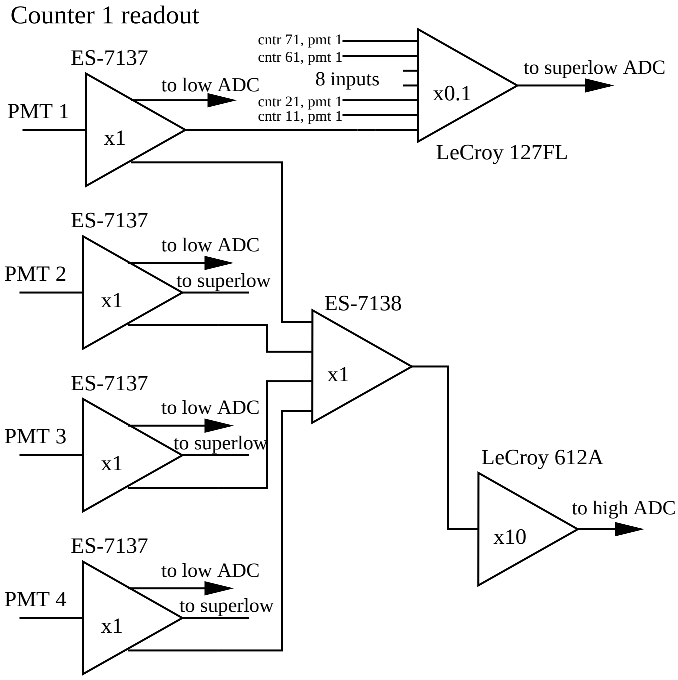

Figure 4: A schematic diagram of the NuTeV calorimeter readout electronics of a counter.

- LOW is the signal from each of the 4 PMT's directly digitized by LeCroy 4300 FERA.
- $SUPERLOW$ signals are the digitized sums of 8 PMT signals which come from 8 different counters, each separated by 10 counters. Each PMT signal is attenuated by 1/10 (fan-in LeCroy 127FL [7]).

A typical minimum ionizing particle signal produces 80 ADC counts in the $HIGH$ channel, 2 ADC counts in each LOW channel, and ~ 0 ADC counts in each $SUPERLOW$ channel. The LOW and $SUPERLOW$ channels are calibrated with respect to the $HIGH$ channels.

Hadronic showers from neutrino interactions deposit up to 600 GeV in the calorimeter (with maximum energy deposition in a single counter of about 100 GeV). A typical hadronic shower in the calorimeter saturates the $HIGH$ channels and leaves a signal of a few hundred ADC counts in the LOW channels. Thus the LOW channels are used to measure the shower energy. In a very small fraction of the time, one of the four LOW channels of the counter is saturated when the transverse position of a neutrino interaction is close to one of the PMT's. In these cases, the attenuated $SUPERLOW$ channel is used.

Calibration of the NuTeV calorimeter begins with the calibration of the readout electronics and tying the $HIGH$, LOW, and $SUPERLOW$ channels into a linear model.

4 Pedestal Subtractions

The best way to determine the pedestal values of the ADC channels well is measuring them under exactly the same conditions as the neutrino data. To achieve this we use two different methods – one using a specially designed random trigger and the other using "quiet regions" of the calorimeter during real neutrino events. A random trigger is activated throughout the run in all gate types to measure pedestals under the same condition as the trigger of interest. The rate of the pedestal trigger is prescaled to provide the necessary number of pedestal events – typically 10 events per accelerator cycle – without overloading the bandwidth.

The second method uses events where the trigger (T2) is designed for neutral current interactions and requires significant energy deposition in consecutive counters in the calorimeter. For each T2 event, an offline analysis program finds "quiet regions" in the calorimeter, using the following algorithm:

1. Count the number of counters with pulse heights more than 1/4 of a MIP (S-bit ON) and reject the event if this number is larger than 10.

2. Select the counters with their own S-bits and the S-bits of their 4 closest neighboring counters OFF.

3. Check that all three readout ADC channels of the selected counters described in Section 3, have energies less than 0.3 MIP. The cut value is chosen to be much less than 1 MIP but much larger than the pedestal; for example in a $HIGH$ ADC channel, one MIP is $\sim$70 ADC counts and a typical pedestal width is $\sim$3 counts, thus the cutoff value of 20 counts is $\sim$7 standard deviations from zero.

4. Use the readouts of each ADC channel of the selected counters as the pedestal values.

The offline analysis procedures use these pedestal events to keep a running average for each electronics channel, using both these methods. The two procedures for measuring pedestals agree to within .015 ADC counts in the LOWs, and .02 ADC counts in the HIGHs. This pedestal uncertainty would contribute a constant term of 32 MeV to the hadron energy resolution if all pedestal differences were correlated, and a 3.6 MeV width if these pedestal differences were uncorrelated. The constant term in the hadron energy resolution is consistent with zero with an error of 110 MeV (see Figure 39). The "quiet region" method is used for neutrino data pedestal subtraction.

Because of the differences in the upstream magnet currents and detector environment, the pedestals during the calibration beam gate and the neutrino beam gate are not necessarily equal. In fact, some channels differ by as much as 0.3 ADC counts in the LOWs. For the analyses of the calibration beam data, we use the random trigger method to measure the pedestals because the upstream part of the calorimeter, where the calibration hadron beam enters, always has energy deposited in every event, precluding the "quiet region" method. The neutrino data pedestal comparisons ensure that this treatment is completely accurate to the few MeV level.

5 Electronics Cross Calibration

Relative calibration of the different channels of electronics is needed because the minimum ionizing particle signal is measured with the $HIGH$ channels, while the neutrino interaction signal is measured with the LOW and $SUPERLOW$ channels. Following the assumption of linearity of all the components of the readout electronics, we assume that the $HIGH$ channel is the linear combination of the 4 LOWs of the same counter:

$$HIGH(i) = \sum_{j=1}^{4} R_j^{hl}(i) \times LOW_j(i), \qquad (1)$$

where i is the counter index, $R_j^{hl}(i)$ is the relative calibration constant between the LOW signal of the PMT j of the counter i and the $HIGH$ signal of the counter i.

The $SUPERLOW$ is the linear combination of the 8 LOWs, as follows:

$$SUPERLOW(i) = \sum_{k=1}^{8} R_j^{sl}(i) \times LOW_j(k), \qquad (2)$$

where i is the $SUPERLOW$ channel number, k is the counter index, j is the fixed PMT index, and $R_j^{sl}(i)$ is the relative calibration constant between the $SUPERLOW$ channel i and the LOW channel of the PMT j of the counter k. The set of calibration coefficients $R_j^{hl}(k)$ and $R_j^{sl}(k)$ is calculated for every data-taking run using the least squares method.

6 Counter Gain Position and Time Dependence

As do all high energy neutrino experiments, NuTeV has an ideal calibration source to track counter gains: muons coming from upstream neutrino interactions in the shielding. This means that not only are the muons completely correlated in time with the actual neutrino beam, but also illuminate the detector in a similar fashion. This section describes how the sample of muons traversing the entire length of the detector during the neutrino beam is used to monitor the position and time dependencies of the individual counter gains.

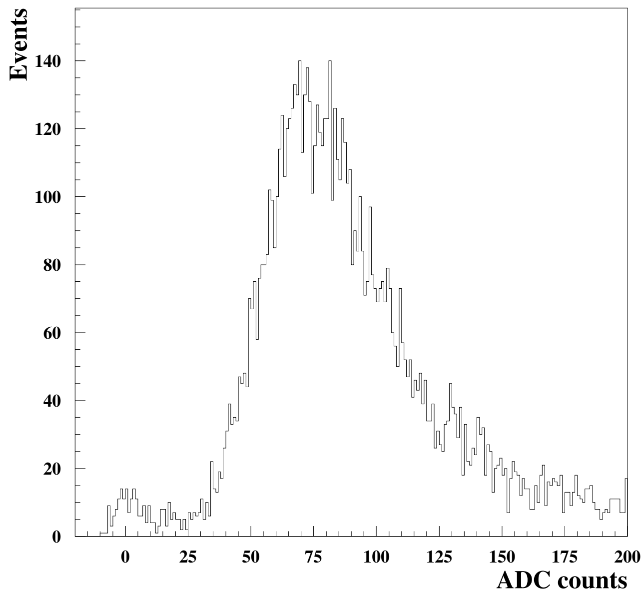

Figure 5: Typical energy deposition of muons traversing one scintillator counter in units of ADC counts.

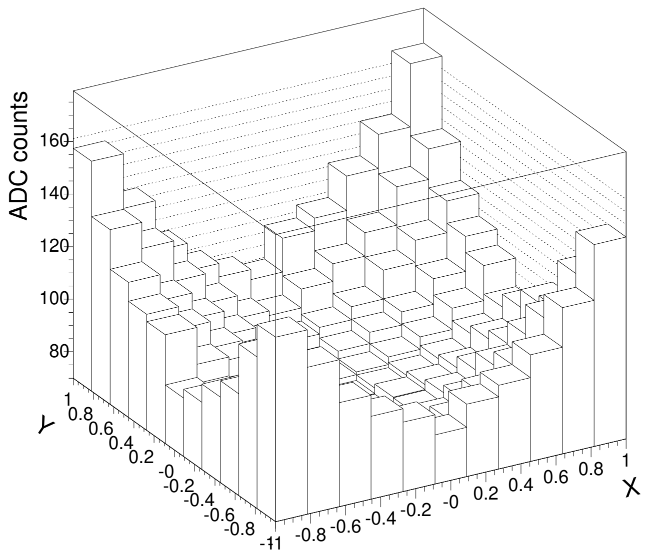

Figure 6: Average counter response to muons traversing as a function of position in the counter. The coordinates are normalized to the half width of the counter, 1.5 m, on both axes.

Figure 5 shows a typical energy deposition profile for muons traversing a particular counter. There are, on average, 30 photoelectrons per MIP per counter. Events with very low pulse heights are from particles that go through the ribs of a counter while the events with large pulse height are from muon bremsstrahlung and e^+e^- pair production. Since pair production increases with increasing muon energy, this energy deposition pattern can be used as an event-by-event muon momentum measurement, as described in Reference 7.

In order to characterize the distribution shown in Figure 5 in a way that is stable with respect to cuts, we use the truncated mean procedure[9]. The truncated mean is determined by calculating the mean of the distribution using all events, then taking the mean again but only including the events between 0.2 and 2 times the previous mean. This procedure is iterated several times until the difference between the mean of two consecutive iterations is less than 0.1% of the previous mean. Corrections are made event-by-event for the muon's momentum as well as the angle with respect to the direction perpendicular to the counter. This procedure provides a "mean" that is insensitive to the width and tails of the pulse height distribution. The truncated mean for 77 GeV muons is defined as 1 MIP.

6.1 Position Dependence

We calculate the average position dependence of the truncated means (which will be referred to as the muon response) for each counter, by averaging over the entire neutrino run. Figure 6 shows that response as a function of position for a typical counter. The light collection is largest at the corners of the counters, near the four phototubes, as expected. The technique used to track the time dependence of the gains alters the position dependence of each counter as a function of time. This is because the gain for each phototube is determined independently as a function of time and is reflected into the position dependence.

6.2 Time Dependence

The gain of a single counter at a particular moment in time during the run depends on the gains of the four phototubes as well as the gain of the scintillator oil itself. To determine the time dependence of the counter gains, we calculate a fractional phototube map, which is defined as the fraction of light reaching a given phototube as a function of position within an independent counter.

These fractional phototube maps are measured using high energy neutrino interactions where the pulse height is high enough to be seen in an individual *LOW* channel. Figure 7 shows two sample phototube maps. Notice that, as expected, the fractional maps are strongly peaked near the phototubes themselves and drop off sharply where two wavelength-shifter bars meet in the center of the counter.

We then fit the muon response over a short period of time to a function with four parameters, where the pa-

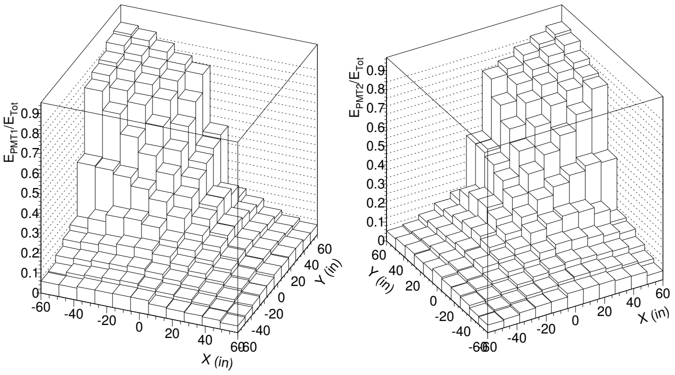

Figure 7: Fractional energy deposition as a function of position for two phototubes in a given counter.

rameters correspond to the gains of the four phototubes. So, if $M^0(x,y,i)$ is the run-averaged muon response map for counter i as a function of x and y, and $F_j(x,y,i)$ is the fraction of light reaching phototube j of counter i, then the run-averaged muon response for phototube j of counter i, $P_j(x,y,i)$, is simply

$$P_j(x,y,i) = M^0(x,y,i) \times F_j(x,y,i). \tag{3}$$

The time-dependent function is then

$$M(x,y,i,t) = \sum_j g_j(i,t) P_j(x,y,i), \tag{4}$$

where $g_j(i,t)$ is the relative gain of phototube j of counter i at time t compared to the average gain over the entire run.

Gains vary by as much as 10% as a function of time and vary, on average, $-0.16\%/^\circ C$ (compared to the value $-0.11\%/^\circ C$ specified by the vendor [14]), as a function of temperature as shown in Figure 8. The temperature dependence varies from counter to counter by $\pm 0.04\%/^\circ C$.

7 Hadron Gain Balance

The technique described in the previous section determines the gain for each scintillator counter relative to all the others, using muons that traverse the entire detector. To set the absolute hadron energy scale of the detector we measure the response of the calorimeter to a monochromatic beam of hadrons incident on the most upstream part of the calorimeter (see Section 12 for details). Since this hadron beam deposits all of its energy in the most upstream 10-12 counters, the hadron response of only those counters is measured. The hadron response measured this way would be usable for the entire calorimeter

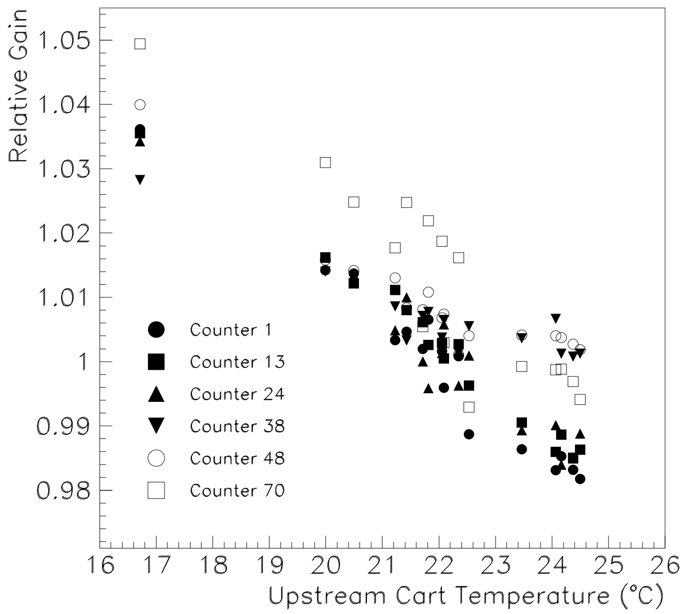

Figure 8: Sum of phototube gain coefficients, normalized to the average gain over the entire neutrino run period, as a function of temperature of the most upstream region of the calorimeter.

if the hadron response were completely correlated to the muon response. However, geometric non-uniformities in the calorimeter give rise to relative differences between the hadron and muon response, breaking the correlation.

The NuTeV calorimeter measures the hadron energy by sampling the shower every 10 cm of steel. The energy deposited by a hadronic shower in the scintillation counters is only a small fraction of the total energy deposited in the detector. Therefore, variations in the passive material surrounding each counter affect the average hadron signal sampled in that counter. In contrast, the muon signal is only dependent on the variations in the active material. Since the relative gain of a counter for hadrons may not be completely correlated with the relative gain for muons, setting the hadron energy scale for the first 10–12 counters is not sufficient to set the scale for the entire detector. In this section we describe the technique used to measure the hadron/muon gain ratio for each counter, using neutrino interactions that occur throughout the entire calorimeter.

Apart from the low interaction rates, neutrinos are a perfect relative hadron calibration source for the entire calorimeter. First of all, if the detector is far enough away from the neutrino production target, the energy distribution of neutrinos interacting in the most upstream counter of the calorimeter is the same as that of the neutrinos interacting in the last counter. In a charged current ν_μ or $\overline{\nu}_\mu$ interaction, which is the majority of neutrino events that NuTeV sees, both a hadron shower and a muon are produced and deposit energy in the calorimeter. As stated previously, the hadron shower deposits most of its energy in the first few counters after the neutrino interaction, while the muon deposits a small amount of energy in each counter over many counters, depending on its angle and energy.

The average measured energy in the calorimeter from neutrino interactions should not depend on where the neutrino interaction occurs, assuming that one always measures the energy by summing over the same number of counters from the event vertex. If one sums over the first 10 counters after the event vertex, then the muon contribution to a 70 GeV shower is about 3%. The additional muon energy deposited in the hadronic shower region would reduce the measured effect, but the amount by which the muon's presence changes the measurement is negligible compared to the statistical uncertainty on the gains.

To determine the hadron/muon gain ratio for each counter, we need a sample of clearly identified neutrino interactions in the calorimeter. Events are selected by requiring a final state muon, visible by a minimum energy deposition extending over at least 20 counters (2 m of steel equivalent) after the event vertex. To remove cosmic ray backgrounds, events are also required to have a reconstructed hadron energy greater than 20 GeV. The hadron energy is determined by summing over the energies of the 10 counters following the event vertex. Since this energy cut ultimately depends on the relative gains obtained from the technique, the procedure must be iterated. The average hadron energy of the events passing all cuts is about 70 GeV.

Events are also required to occur at least 4 counters from the upstream end of the calorimeter, 20 counters before the downstream end of the calorimeter, and within 1.27 m of the center of the detector. These fiducial cuts ensure that the event is not induced by a charged particle entering from the side or front of the detector, and that the hadronic shower in the event is fully contained within the calorimeter. Because of these fiducial volume cuts, we are unable to use this technique to determine the relative gains of the 15 most downstream or 4 most upstream counters. However, the most upstream counter hadron/muon gain ratios are determined using a similar technique, described here, with the calibration beam hadron data. The first four counters' gains are set by comparing the calibration beam hadron response of showers starting in the most upstream set of four counters with those in the next set of four counters that are immediate downstream of the first set and whose gains have been determined from the neutrino data.

The fitting procedure constrains the hadron energy of neutrino interactions to be constant by varying the relative gains of the counters. Let the visible hadron energy of a neutrino event that starts in counter i be denoted as

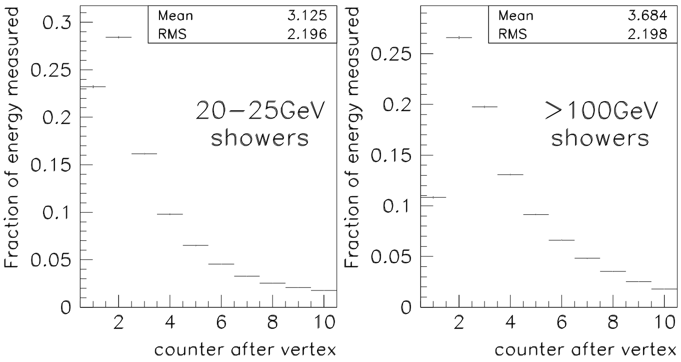

Figure 9: Average longitudinal hadronic shower profiles of neutrino events in two different shower energy ranges. It can be seen from the plots that large fraction of shower energy is deposited in two to three consecutive counters.

$EHAD_i$. In a given event the individual counter energies using the muon-derived gains are denoted by $E(j)$, and the hadron/muon gain ratio for each counter is denoted by h_j. In this notation,

$$EHAD_i = \Sigma_{j=i}^{i+9} h_j E(j) \tag{5}$$

where the sum over 10 counters (1 m of steel equivalent) is expected to include more than 95% of the hadronic shower. The average hadron energy over all neutrino events that occur in counter i is then

$$\begin{aligned} < EHAD_i > &= < \Sigma_{j=i}^{i+9} h_j E(j) > \\ &= \Sigma_{j=i}^{i+9} h_j < E(j) > \end{aligned}$$

Thus in theory the average hadron energy of showers that start in counter i depends not only on counter i's gain but also on the gains of the nine subsequent counters. In practice, however, hadron showers deposit a large fraction of their energy in only two or three consecutive counters around the shower maximum, as shown in Figure 9.

One first computes the average hadron energy ($EAVE$) over the entire fiducial volume by setting all the initial gains h_j to unity, making the cuts described above, and calculating the average $EHAD_i$ over all the events that pass the cuts. Then, one can fit for the hadron gains by minimizing a χ^2, where the χ^2 is defined as follows:

$$\chi^2 = \Sigma_{i=20}^{80} \frac{(EHAD_i(g_i, g_{i-1}, g_{i-2}...) - EAVE)^2}{ERR_i^2} \tag{6}$$

and the ERR_i^2 is defined as:

$$ERR_i^2 = (< EHAD_i^2 > - < EHAD_i >^2)/N_i \tag{7}$$

where N_i is the number of neutrino events, passing all cuts, that start at counter i, and the error is calculated

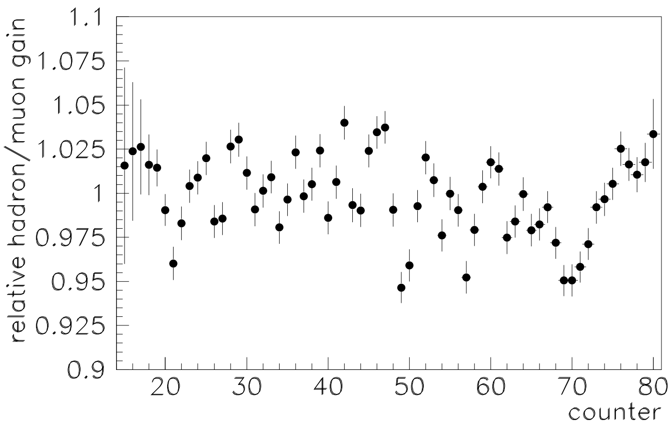

Figure 10: Relative hadron/muon counter gains which arise from detector non-uniformities unrelated to scintillator thickness.

assuming the gains h_j are all set to their initial values (which for the first pass is simply unity). To fit for the gains, in theory, one simply has to minimize the χ^2 defined in Eq. 6, determine the gains, and then iterate, making the energy cut and re-computing the new average and errors using the gains from the previous iteration.

In fact the χ^2 defined in Eq. 6 is unstable, due to the fact that a hadron deposits most of its energy in two or three consecutive counters at the shower maximum and this causes a strong correlation between the two counters next to each other. The χ^2, when computed this way, is low not only for uniform gains very close to 1 but also for gains which are staggered by a certain amount, where the even counters are all high and the odd counters are all low (or vice versa). This variation in hadron gains is larger and more regular than would be expected from detector non-uniformities in thickness and composition of material. This artificial hadron gain variation is avoided by separately fitting the gains using events whose showers start in every other counter (for example, even-numbered counters), then using the complementary set of events (for example, showers starting in odd-numbered counters) and refitting. The resulting gains for all counters are consistent between the two fits, have smaller errors than when all showers are included at once, and are much closer to unity.

By averaging the two fit results and iterating, the gains are stable to better than 0.2% after 3 iterations. The statistical uncertainty on each relative gain is about 0.9%, and is larger near the downstream edge of the detector where there are only events starting upstream of those counters. Figure 10 shows the gains obtained after four iterations using the technique described in this section. The gains have an RMS of 2.3%, and are consistent with geometrical non-uniformities in the calorimeter (water bag thicknesses, steel plate thicknesses, etc.).

The relative hadron gains allow a determination of the absolute hadron energy scale of the entire calorimeter by measuring the response of the upstream most counters to a monochromatic beam of hadrons. The total statistical uncertainty on the hadron gains in the overlap region where there is both calibration beam and neutrino data is equal to 0.4% and dominates the overall uncertainty in the hadron energy scale. Each counter's hadron/muon gain ratio uncertainty (0.9%) is uncorrelated between the counters. The contributions of this uncertainty to the calibration beam energy measurement is reflected in the uncertainty in hadron response measurement and is negligably small due to statistically random longitudinal development of hadron showers (see Section 12).

The relative gains obtained using the technique described in this section are used for the energy reconstruction in both the hadron and electron response measurements.

8 The NuTeV Calibration Beam

NuTeV is designed to include a simultaneous calibration beam separated from the neutrino beam by 1.4 seconds, yet running within the same one-minute accelerator cycle (see Figure 11). The calibration beam is used to set the absolute energy scale of the experiment, and also to measure the response of the calorimeter to hadrons, electrons, and muons, in order to properly simulate the detector. Finally, the calibration beam is instrumental in monitoring the time dependence as measured by the muon map technique described in Section 6.

The calibration beam period within a cycle is 18 seconds, and the typical beam incident angle to the center of the NuTeV calorimeter is 43 mrad in the horizontal direction (0 mrad in vertical) with respect to the centerline of the calorimeter. The calibration beamline can transport particles of energies from 4.8 GeV to 190 GeV, and depending on the beamline apparatus and magnet settings, can produce high purity beams of electrons, hadrons, or muons for energies above 30 GeV.

The beamline is instrumented as a low mass spectrometer with a long lever arm. The distance between the most upstream chambers in the spectrometer and the momentum-analyzing magnets is 83.3 m, and the distance between the most downstream chamber and the magnets is 69.2 m. This separation allows a modest alignment uncertainty of 1 mm to translate into only a 0.1% uncertainty in the absolute momentum scale. The event-by-event resolution of the spectrometer, dominated by multiple scattering, is better than 0.3% for most energies. The beamline instrumentation is augmented for some of the run with a removable Čerenkov detector and a TRD array used to measure the beam particle composition.

Over the course of the experiment, standard runs

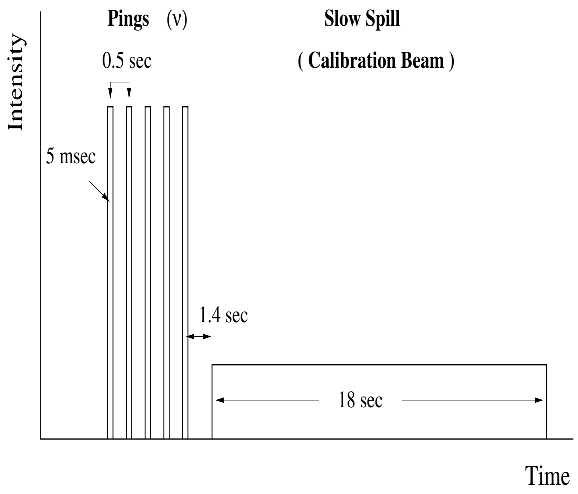

Figure 11: Accelerator time structure. Note that the interval between the last neutrino ping and the slow spill calibration beam is only 1.4 seconds, allowing essentially an *in situ* calibration.

were taken at least once a week (50 and 100 GeV hadrons) and hadron energy scans between 4.8 GeV and 190 GeV were taken once a month. Overall, NuTeV accumulated a total of 17 million test beam triggers.

8.1 Beam Time Structure

The accelerator time structure during the 1996-97 Fermilab fixed target run is depicted in Figure 11. The accelerator complex cycles every 60.1 sec. The neutrino beam is delivered in five fast resonance extraction pulses ("pings") of 5 msec width. The pings are separated by 0.5 sec. The NuTeV slow spill calibration beam begins 1.4 sec after the last ping and has a duration of 18 sec with uniformly distributed beam intensity. This calibration beam is delivered in a beamline that is completely independent from the fast spill. This time structure provides continuous calibration data, taken concurrently with the neutrino beam, and allows for an *in situ* calibration of the detector.

8.2 Beam Selection Scheme

The NuTeV calibration program involves electrons, hadrons, and muons of momentum ranging from 4.8 GeV to 190 GeV. In order to select the desired type of particles for a specific program with high purity, the beamline is designed as shown in Figure 12.

The target (NT8TGT) in the calibration beam is a 7.5 cm (W) $\times$ 7.5 cm (H) $\times$ 30.3 cm (L) aluminum block. Protons of 800 GeV momentum strike the target with an integrated intensity between 4×10^{11} and 8×10^{11} protons on target throughout the 18 second long slow spill. The secondaries are then focused by a set of quadrupole magnets (NT9Q1 and NT9Q2) to the enclosure NTA and

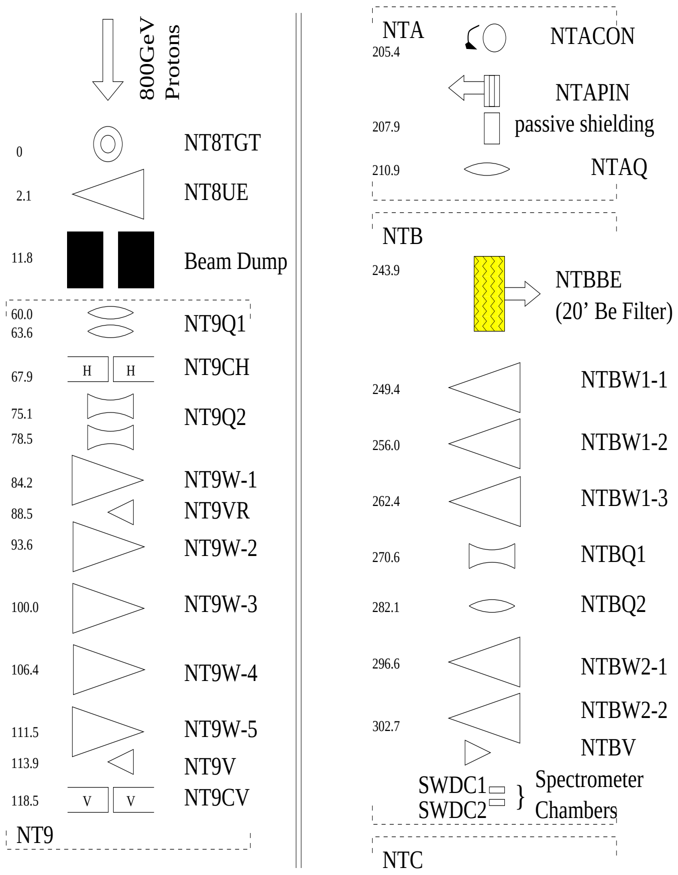

Figure 12: NuTeV calibration beamline schematics. The "Ferris wheel" (NTACON) with four different thickness converter material is used to select pure hadrons or electrons. The 6 m long Be filter(NTBBE) is used to select pure muons. The numbers on the left-hand-side of each component indicate the relative distance of the component to the primary target (NT8TGT) in meters. Some beam position and intensity monitoring devices are not drawn in this figure because they are irrelevant for this paper.

collimated by a horizontal collimator (NT9CH) whose opening is adjusted depending on particle type and intensity. The polarity of the beamline is set to direct negatively charged particles to reduce intensity.

The horizontal collimator (NT9CH) is then followed by a string of dipole magnets (NT9W-1, 2, 3, 4, and 5), fed by one power supply, for initial momentum selection, bending the beam in the horizontal plane. The vertical collimator (NT9CV) following the first set of dipoles (NT9W's) is used to further cut down the intensity.

The "Ferris wheel" (NTACON), located immediately downstream of the set of collimators and the initial momentum selection dipoles, has four mounts, each placing a different thickness of material into the beam at a time. The thicknesses correspond to an empty hole, $0.2X_0$, $6X_0$, and $12X_0$. The empty hole is used for the muon mode, while the $0.2X_0$ piece is used for the electron mode. In the electron mode, the magnets downstream of

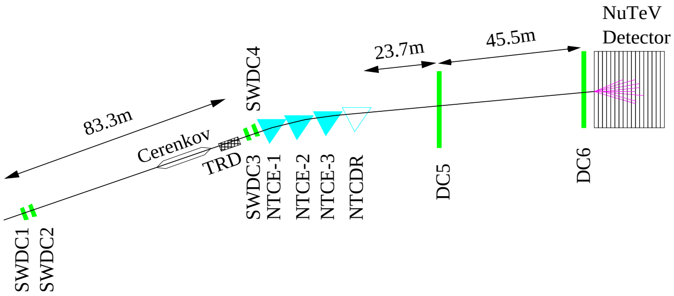

Figure 13: A schematic view of the NuTeV calibration beam spectrometer system. The large distances between the chamber stations allow accurate absolute momentum determination.

the "Ferris wheel" are tuned for 20% lower momentum particles to compensate electron energy loss in the material. The two higher radiation length materials are put in the path of the beam for hadron modes to eliminates electrons from the beam. The thicker material is used for higher energy beams, the thinner for lower.

The pinhole collimator (NTAPIN) following the "Ferris wheel" is put in the beam only for higher energy hadron modes ($E > 30$ GeV) to further cut down intensity and increase radiation safety. Typically, the size of the hole in the pinhole collimator is 5 mm $\times$ 5 mm and the momentum bite set by this collimator opening is approximately 0.2 GeV.

The 6 m long beryllium filter (NTBBE) is only used in muon modes to filter out hadrons and electrons in the beam. The energy loss of muons in the filter is approximately 6% while the survival probabilities of hadrons and electrons through the filter are less than 3.4×10^{-7} and 3.5×10^{-8}, respectively. The filter is then followed by additional two sets of dipoles (NTBW1-1, 2, 3, NTBW2-1, and 2) for further refinement of momentum selection. This combination of three large dipole strings throughout the long stretch of the beamline removes virtually all possible contamination of unwanted particles and momenta.

A final precision spectrometer is used to determine the beam momentum on an event-by-event basis. The spectrometer begins with two small area drift chambers (SDWC1 and SDWC2 in Figure 12) positioned at the downstream end of the last dipole string in the same beam enclosure (NTB). Figure 13 shows a schematic view of the NuTeV calibration beam spectrometer system. The particle ID system, which consists of a Čerenkov counter followed by an array of TRD's, is located just upstream of the second set of chambers which, in turn, were positioned immediately upstream of the spectrometer dipole magnet string. When particle identification is not needed, these detectors are rolled out of the beamline and are replaced by a vacuum pipe to reduce multiple scattering.

The last dipole in the spectrometer magnet string

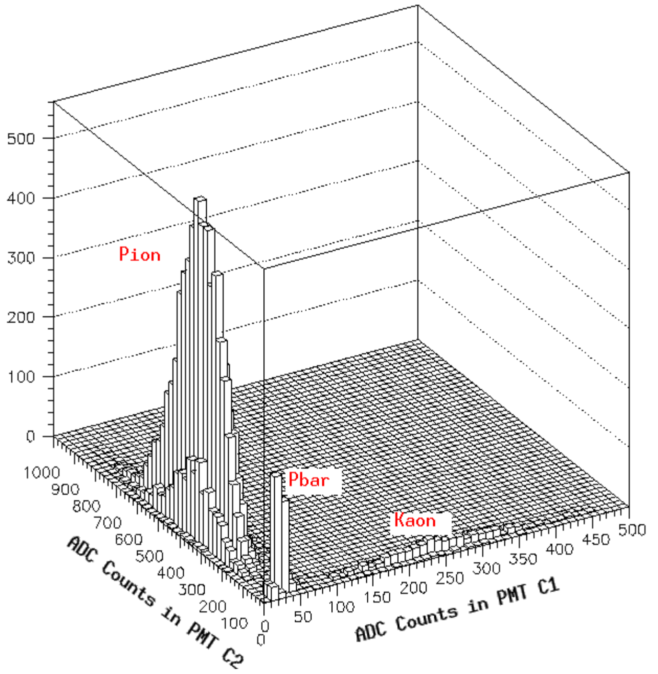

Figure 14: PMT signals of the Čerenkov counter with a 160 torr nitrogen gas. A clean particle separation between $\pi(C_1)$, K(C_2), and $\overline{p}$(ped) at 50 GeV is apparent.

can be rotated. This dipole is an integral part of the spectrometer for beams with energies greater than or equal to 120 GeV and is also used to direct the beam to various positions on the detector surface for position dependent response measurements.

8.3 Particle Identification and Beam Purity

The Čerenkov counter provides particle identification for pions, kaons, anti-protons, and electrons, depending on the type of gas and the threshold pressure for each type of particles. The Čerenkov counter is equipped with two PMT's, C_1 and C_2, placed to face opposite directions, and is designed to act as a differential Čerenkov counter. The PMT C_1, accepts low angle (< 4.5 mrad) Čerenkov light from heavy particles, while the PMT C_2, accepts large angle light from lighter particles of the same momentum.

Figure 14 demonstrates the excellent particle identification for anti-protons, kaons, and pions within the 50 GeV hadron beam using the Čerenkov counter under nitrogen, at a pressure of 160 torr. While the small signal in the pedestal region is dominated by anti-protons, it could also be contaminated by other particles due to inefficiencies in C_1 and C_2. An inefficiency study, performed by counting the number of pedestal events for the clean muon sample with Čerenkov pressure above the muon threshold, shows that the C_1 and C_2 inefficiencies are

P (GeV)	Electron fraction(%)	Hadron fraction(%)
5	92	8
7.5	72	28
15	66	34 (π^-:95.6, $\overline{p}$+K$^-$:4.1)
20	< 1	> 99 (π^-:95.5, $\overline{p}$+K$^-$:4.5)
30	< 0.25	> 99.75 (π^-:94.9,$\overline{p}$+K$^-$:5.1)
50	0	100 (π^-:93.9, K$^-$:3.1, $\overline{p}$:3.0)
75	0	100 (π^-:91.7, K$^-$:5.1, $\overline{p}$:3.2)
120	0	100 (π^-:91, K$^-$:6.2, $\overline{p}$:2.8)

Table 2: Summary of particle composition ($e^-/\pi^-/\mathrm{K}^-/\overline{p}$) in the hadron calibration beam for various energies.

less than 0.24% and 0.008%, respectively.

Table 2 summarizes the beam particle composition for various hadron tunes. It is well demonstrated that the contamination from electrons in the beam for hadron tunes of momentum greater than 30 GeV is less than 0.25%, minimizing the systematic error in hadron response measurements.

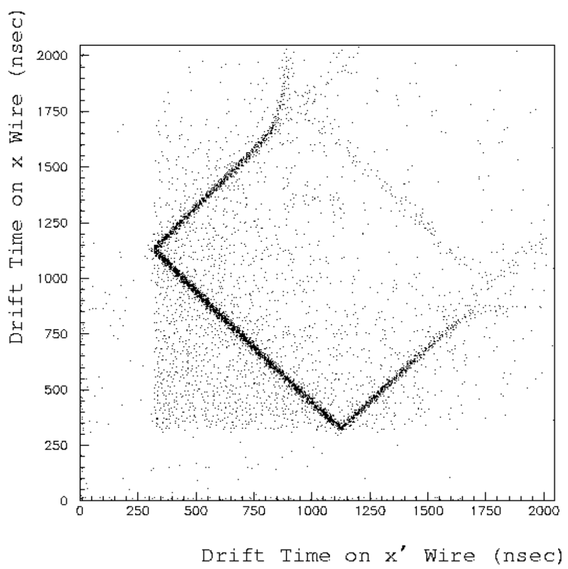

Figure 15: T_1 vs T_2 for $x-$view of an SWDC plane. The cluster of points along the line with slope -1 to the left corresponds to the region between the x and x' wires; these events are used for track fitting. Nonlinear time-to-distance effects are visible for very long drift times and for events very close to the sense wires.

8.4 The Calibration Spectrometer

The spectrometer is designed to measure the absolute momentum of the calibration beam particles to better than 0.3% in an event-by-event basis. This is accomplished by two means. First precisely calibrated dipole magnets are used, with $\int Bd\ell$ known to better than 0.1% in the region traversed by the beam. Also, the bend angle is measured to better than 0.1% using drift chambers positioned over the 500 m beamline, which provides a long lever arm. This long length of the spectrometer chamber spacing allows us to tolerate a relative chamber alignment uncertainty of $\sim 100\ \mu$m.

8.4.1 Upstream Tracking

The position and the angle of the calibration beam tracks are determined at the upstream end of the spectrometer magnet by four 12 cm $\times$ 12 cm Single Wire Drift Chambers (SWDC)[10]. Each chamber consists of a pair of sense wires offset by ± 2.03 cm from the beam center in each view. The operating gas, an equal mixture of Ar and C_2H_6, and the field-shaping wires provide a saturated 49 μm/ns drift speed over most of the gas volume. This can be seen in Figure 15, where the drift times measured on the two sense wires are plotted against each other. The dark band with slope -1 is produced by tracks passing between the two wires. The two bands with slope $+1$ are produced by the tracks passing on the same side of the two wires. Small non-linear drift effects can be seen at very long and very short drift times. These effects are eliminated by using only tracks passing between the two wires.

The chambers are grouped in two stations of two SWDC's each. One station is located immediately upstream of the most upstream spectrometer magnet and the other is 83.3 m upstream of that station.

Chamber position resolution can be determined by measuring the width of the distribution of differences in position measurements for a track passing between the two sense wires, and then dividing by $\sqrt{2}$. This is shown in Figure 16, which demonstrates that the chambers have a resolution of 300 μm. Chamber alignment is achieved through an initial optical survey to an accuracy of 50 μm. The integrity of the alignment is constantly checked using the straight test beam tracks, with the spectrometer magnets removed from their normal positions. Residual misalignments are estimated to be $\leq 100\ \mu$m and make a negligible contribution to slope and intercept measurements.

Figure 17 shows the distribution of slope, intercept, and χ^2 for a typical upstream sample of tracks in each view. Tracks enter the spectrometer at projected angles of $\theta_x = 74$ mrad, $\theta_y = -0.3$ mrad with angular spreads of $\sigma_x = 0.2$ mrad, $\sigma_y = 0.08$ mrad. The width of the beam is approximately 2.5 cm in x and y and is set by the trigger paddles. The χ^2 distributions are consistent with their expected shape, giving us confidence that the upstream tracking is well understood.

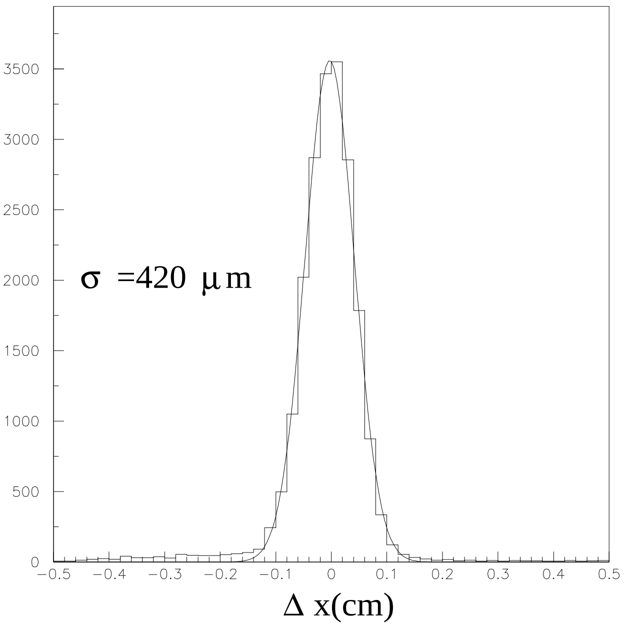

Figure 16: Difference in coordinates, $X_1 - X_2$ for an SWDC chamber plane from a sample of calibration beam tracks. The solid line represents a Gaussian fit on the distribution. The σ of this distribution is 420 μm, implying a spatial resolution of 300 μm.

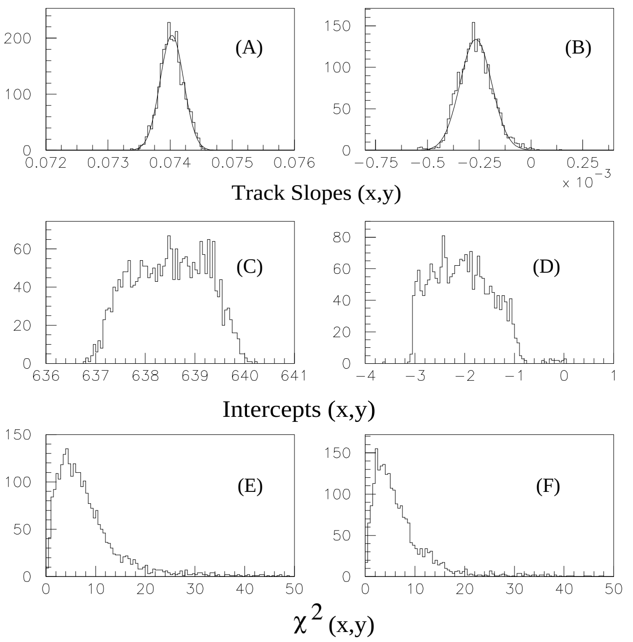

Figure 17: A and B: Track slopes in x and y at the upstream end of calibration spectrometer magnets as determined by chamber tracking. C and D: Beam profile in x and y at the upstream end of calibration spectrometer magnets as determined by chamber tracking. E and F: χ^2 distribution of the upstream chamber fits in x and y views. Both distributions follow the expected normal χ^2 distributions.

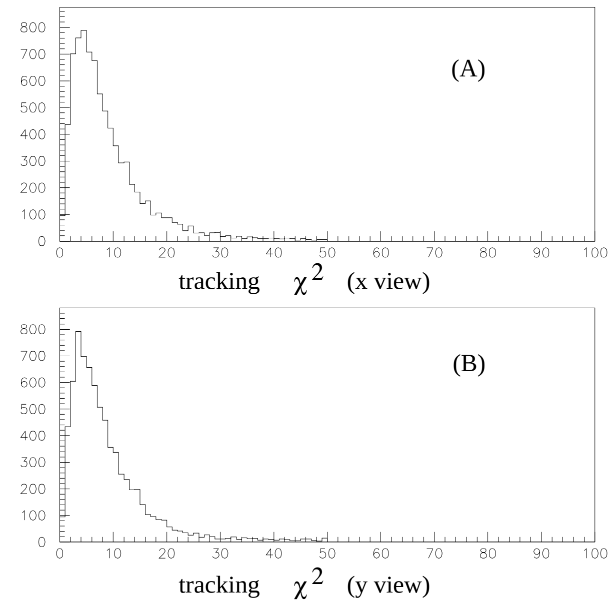

Figure 18: χ^2 distribution for X (A) and Y (B) view of calibration beam spectrometer track fit using chambers upstream and downstream of the spectrometer magnet string. Ten points are used in the three parameter fit.

8.4.2 Downstream Tracking

The downstream section of the spectrometer consists of two 3 m × 3 m three-wire drift chambers separated by 45.5 m. The first chamber downstream of the spectrometer magnet string is positioned 23.7 m from the downstream end of the last momentum analyzing magnet. Figure 18 shows the χ^2 distributions of the spectrometer tracking fit, using the chambers upstream and downstream of the spectrometer dipole magnets. The fact that these distributions follow the expected χ^2 distribution gives us confidence in the absolute momentum determination.

8.4.3 Spectrometer Magnet Calibration

The Fermilab Magnet Test Facility (MTF) calibrated the five EPB dipoles [11] (four plus an unused spare) used in the spectrometer. Precise $\int B d\ell$ data are taken at the centerline of the magnet and are tied to magnet current and Hall probe voltage readout recordings. Shape studies are performed for $\int B d\ell$ vs horizontal position at fixed vertical position and magnet shunt current measurements [12]. Data are summarized by polynomial fits to the $\int B d\ell$ measurements as functions of both Hall probe output and magnet current.

While shunt devices can be internally calibrated to better than 1 part in 10^4, the current reading in the two different configurations (i.e. different power sup-

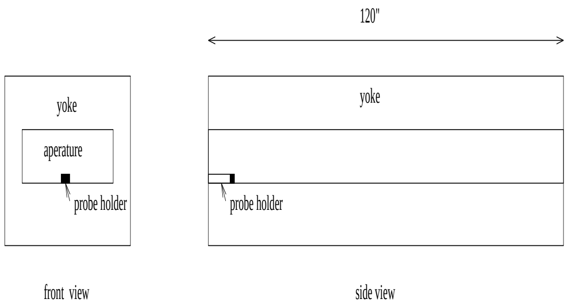

Figure 19: A schematic diagram of the Hall probe and the holder location inside the magnet.

Magnet	Probe	$\mathbf{A_1}$ (m)	$\mathbf{A_0}$ (T·m)	$\mathbf{A_2}$ ($\mathrm{T^{-1}}$·m)
11243	95421	-3.03617	-0.00517	0.00574
11243	95420	-3.04009	-0.00438	0.00283
11243	95422	-3.03576	-0.00448	0.00130
11243	95423	-3.03392	-0.00276	0.00056
11459	95421	-3.03770	-0.00491	0.00046
11632	95421	-3.03575	-0.00532	0.00078
11694	95420	-3.03983	-0.00351	0.00066
20015	95421	-3.04207	-0.00473	0.00051

Table 3: Coefficients of fits to $\int Bd\ell$ vs Hall probe readout for different calibration spectrometer EPB dipole/Hall probe combinations. The fits are of the form $\int Bd\ell = A_0 + A_1 H + A_2 H^2$, where H is the Hall probe readout in Tesla and $\int Bd\ell$ is in units of Tesla-meters.

plies, buses, cables, and shunts) may differ by substantially more and cannot be used to obtain the absolute $\int Bd\ell$. Therefore, the absolute $\int Bd\ell$ is determined in the data taking configuration based on the Hall probe versus $\int Bd\ell$ calibration data. Further details of the magnet calibration are described elsewhere[13].

Each of the four Hall probes is attached to a probe holder before the holders are mounted in the magnets. The probe holders are located approximately in the center magnet aperture on the lower pole face near the magnet opening. This is shown schematically in Figure 19. Holders are angled to keep the probe cables from interfering with the beam and vice versa. Hall probes are read out and the values are recorded by the NuTeV data acquisition system once per spill, and $\int Bd\ell$ data are calculated for all events within a given spill using quadratic fits to the MTF Hall probe calibration data.

Table 3 summarizes the $\int Bd\ell$ vs Hall probe fits to the data. The $\int Bd\ell$-Hall probe relationship is very nearly linear, with the offset and quadratic corrections (A_0 and A_2 in Table 3) only a few parts-per-mil of the linear calibration constants A_1. Figure 20 compares the coefficient A_1 for different probe-magnet combinations; variations from dipole-to-dipole and probe-to-probe are at the few tenths of a percent level. Linear fits do not

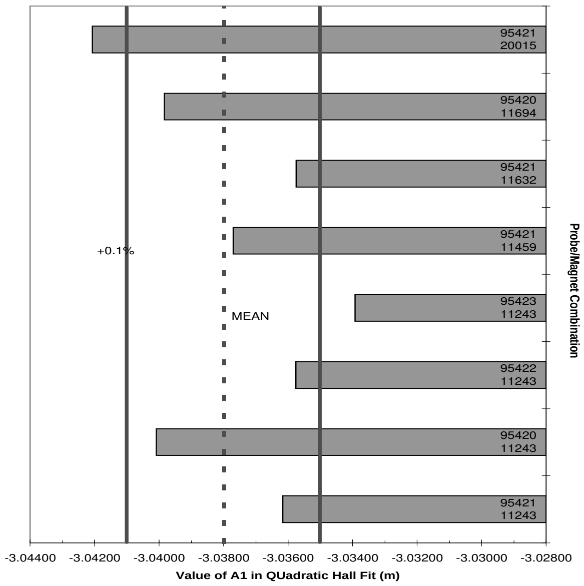

Figure 20: Comparison of linear coefficients in $\int Bd\ell$ vs Hall probe readout for different EPB dipole/ Hall probe combinations for the NuTeV calibration beam spectrometer magnets.

parameterize the data to the required accuracy ($\leq 0.1\%$ deviation), but quadratic fits well describe both polarities of current ramping. Figure 21 shows the fit results superimposed on the data for one of the magnets; plotted are the $\int Bd\ell$ points divided by the probe readout in order to accentuate non-linear effects.

As a check, $\int Bd\ell$ values have also been calculated from high-order polynomial fits to $\int Bd\ell$ vs magnet shunt current data taken at MTF. Figure 22 compares the Hall probe determination to the shunt current determination of three spectrometer magnets for a typical run. The two determinations agree within the expected precision of the shunt current measurement.

8.5 The Calibration Trigger

The calibration beam trigger consists of two small scintillator paddles shaped to shadow the "good field" regions of the spectrometer magnets. The two paddles are positioned immediately upstream and downstream of the momentum analyzing magnet string. Figure 23 shows a schematic diagram of a calibration beam trigger scintillator paddle. The "good field" region, mapped out with $\int Bd\ell$ measurements described above, consists of the region across the face of the magnet over which the $\int Bd\ell$ varies by less than 0.1% from its value at the center of the magnet. This unbiased trigger, with no energy requirement in the calorimeter, automatically maintains the 0.1% tolerance on the $\int Bd\ell$.

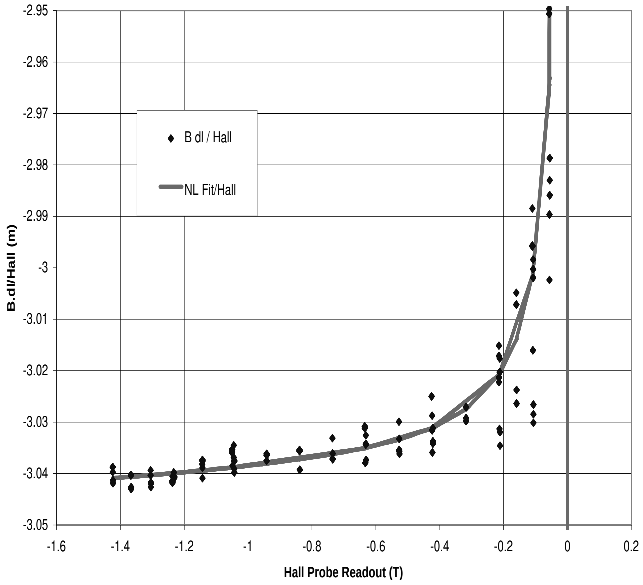

Figure 21: Results of quadratic fit to $\int Bd\ell$ vs Hall probe readout for a typical EPB dipole in the NuTeV calibration spectrometer. $\int Bd\ell/H$ vs H, where H is the Hall probe reading in Tesla and $\int Bd\ell$ in Tesla-meters is plotted to show the non-linear region at low fields.

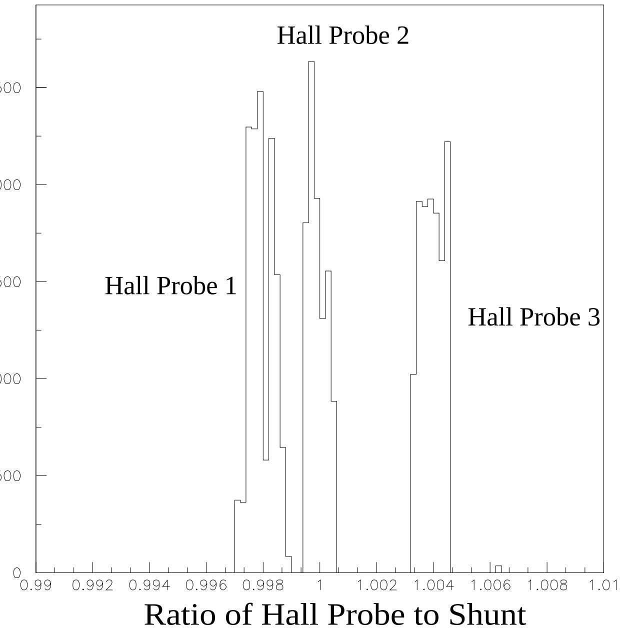

Figure 22: Ratio of $\int Bd\ell$ calculated from magnet shunt current to the value calculated from the Hall probe for a typical NuTeV calibration run.

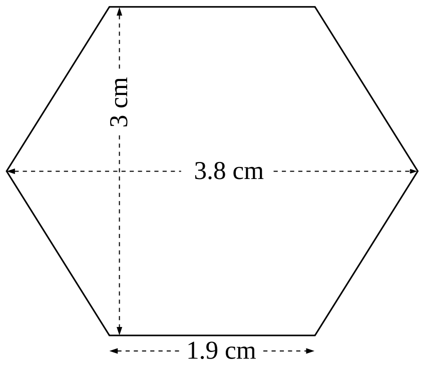

Figure 23: A schematic drawing of the NuTeV calibration beam trigger scintillation paddle.

9 Corrections for Systematic Effects

In order to achieve sub-per cent precision in the absolute energy scale calibration, it is necessary for NuTeV to take into account a number of systematic effects. Most of these are due to the fact that the gains of the calorimeter are determined using muons from the neutrino beam which averages the detector response over a long period of time (typically a week or more), while the calibration beam runs take place over much shorter time periods; for example, some hadron energy tests run for as little as an hour. The time dependent effects that need to be taken into account and that are discussed in this section are high voltage and temperature gain dependencies.

There are other differences between the energy deposition from a neutrino interaction and that from an incoming beam of particles. One of the differences is the calibration beam composition. The particle type dependence of the energy deposition is studied, and correction for the anti-proton contamination is applied for final energy scale calibration.

Another difference between neutrino and calibration beam energy deposition arises from the fact that a neutrino may interact at different distances from a scintillation counter, whereas the calibration beam always enters the calorimeter at the front and, in particular, electrons always interact in the first counter, which is preceded by two inches of steel. For this reason special care is taken to ensure that the calibration of the first few counters in the calorimeter is consistent with that of the latter ones.

9.1 Environmental and Voltage Monitoring System

In order to obtain corrections for systematic effects, temperature, pressure, humidity, high voltages, and low voltages are monitored locally by a microprocessor controlled system. This system communicated periodically with the data acquisition computer to record the monitored data on the same tape as the neutrino and calibration data. The period for recording this data is one beam cycle, about one minute.

The microprocessor signals were digitized by a 12-bit ADC and then read into a Basic Stamp BS2 microprocessor. The signal is averaged over many readings to avoid noise. The results of this averaging were transmitted via a standard serial communication network to a personal computer in the control room. The personal computer monitored these values, issued warnings when values began to deviate from the standard, issued alarms when the values were out of limits, and transmitted the raw data to the data acquisition system to be written to tape.

The temperature of the calorimeter is monitored with a digital temperature integrated circuit to a resolution of $\pm 0.6°C$. The temperature probes are placed in four locations on every fourteenth calorimeter counter unit. The absolute atmospheric pressure is monitored in four locations with a resolution of $\pm 1.5\%$. The other environmental variables are monitored to a resolution of $\pm 2\%$ in several places throughout the experimental hall.

The calorimeter PMT high voltages are monitored using the LeCroy 1440 main frame readout system. The readout is recorded once per cycle to the data tape together with neutrino and calibration data.

9.2 Beam Component Correction

The absolute hadron energy scale of the calorimeter is determined by measuring its response to single pion interactions. Any difference in the response of the detector between pions and the kaons or anti-protons which contaminate the calibration beam must be accounted for when the absolute energy scale is set. These differences in the calorimeter response are investigated using clean samples of each particle type using the Čerenkov counter information.

Based on the studies using the hadron beam at various energies, we find that the calorimeter response to kaons agrees with that of pions. However, showers from anti-protons show higher responses (by $\sim$1 GeV) than the showers from pions, due to the $p\overline{p}$ annihilation at the end of shower development process. This effect has been discussed in a previous calorimeter review [15].

At high energies ($\geq$ 50 GeV), the anti-proton effect is found to be negligible ($< 0.03\%$), while this effect is very important at low energies. Table 4 summarizes the sizes of the correction factors, the contamination of kaons, anti-protons, and the shower responses (normalized to the pion shower response) of the calorimeter.

P (GeV)	shower response (normalized to pion)	fraction (%)	correction to E_{had} (%)
5	$\overline{p}$ 1.2	3±1	-0.6±0.2
10	$\overline{p}$ 1.1	3±1	-0.3±0.1
15	$\overline{p}$+K$^-$: 1.054 ± 0.017	4.1	-0.22
20	$\overline{p}$+K$^-$: 1.033 ± 0.010	4.5	-0.15
30	$\overline{p}$+K$^-$: 1.027 ± 0.006	5.1	-0.14
50	$\overline{p}$: 1.011 ± 0.006 K$^-$: 0.995 ± 0.006	3.0 3.1	-0.017
75	$\overline{p}$: 1.008 ± 0.004 K$^-$: 0.997 ± 0.004	3.2 5.1	-0.010
120	$\overline{p}$: 1.005 ± 0.004 K$^-$: 0.998 ± 0.003	2.8 6.2	-0.002

Table 4: Hadronic shower responses from kaon and anti-proton normalized to that of pions, and the correction factors to the hadronic shower energy, especially due to the anti-proton effect.

9.3 Muon Radiative Equilibrium (RE) Correction

When a muon traverses material, it loses energy via electromagnetic processes: knock out electrons (δ-ray) from atoms, bremsstrahlung, e^+e^- pair production, etc. While most of the knock-on electrons are low energy electrons that do not penetrate deep into the material, high energy electrons from muon energy loss processes can leave energy in several counters. Thus, the energy deposited in the most upstream few counters in the NuTeV calorimeter is relatively lower than other downstream counters since they have less material in before them. This effect is called the radiative equilibrium (RE) effect. Since the NuTeV calibration beam enters the detector striking the most upstream counters, and the gain corrections for the counters are determined relative to muon energy deposit in a given counter, it is necessary for analyses to apply corrections to the gain factors to account for the RE effect. This effect causes an artificial over-estimate of the energy deposited in a few upstream counters relative to the downstream ones.

We determine the size of this correction using a high statistics GEANT Monte Carlo study. Since this effect reduces the muon energy deposit gain normalization factors for the most upstream and the second most upstream counters by 1% and 0.4%, respectively, the normalized hadron energy deposit in these two counters need to be reduced by the same factors. The resulting overall size of this correction to the hadronic response is less than 0.1%.

9.4 Temperature Correction

Many characteristics of the NuTeV calorimeter – PMT high voltage, PMT quantum efficiencies, scintillator light yield, electronics noise, etc – change with temperature. These changes contribute to the temperature dependence of the overall gain. Separating systematic effects from these different sources is difficult and unnecessary. The net effect that the temperature has on the overall gains of the PMT's can be measured by muon response maps and the average temperatures for each of these muon maps. That temperature dependence is shown in Figure 8 in Section 6.

The muon map of the counter for a given running period is the time-integrated, beam-weighted response of the counter for a particular period of time. Since the neutrino data itself is, by definition, beam-weighted, the "average temperature" for a muon map is also the average temperature for the neutrino data.

However, this is not true for calibration beam data. A particular calibration beam study might only take a few hours, while the average muon map is calculated over a few weeks. If, during the few hours of the calibration beam study, the temperature is significantly different from the average temperature for the muon map used, the gain of the calorimeter during that brief time interval would be different from the muon map average gain. To correct for these gain differences, a temperature correction is applied to the calibration beam data on an event-by-event basis, such that the effective muon map used would be the appropriate muon map for that particular temperature.

To calculate the corrections, the average gain for each counter ($G = \frac{g_A+g_B+g_C+g_D}{4}$) is linearly correlated to the measured temperature from the sensors located on the calorimeter ($G(T) = A \times T + B$). Although there are sensors placed along the length of the calorimeter and the temperatures are measured throughout the experimental hall, the temperatures measured by the sensors near the least insulated part of the calorimeter are used to determine the temperature correction. The temperature correction to each counter is simply the first term in the Taylor expansion of ratio of $G(T_{muon\ map})/G(T_{current})$, or $(1-\frac{B}{A}\times(T_{muon\ map}-T_{current}))$. Temperature corrections tend to be as large as several tenths of a percent.

9.5 High Voltage Correction

Counters in the NuTeV calorimeter have four PMT's, one in each corner, as described in Section 2. The overall gain of a given counter depends strongly on the combination of the individual PMT gain. One of the systematic factors that directly affects the gain is PMT high voltage (HV). Thus, for a high precision calibration, it is important to correct for overall gain fluctuations due to any HV variation.

The PMT gain variation as a function of HV is measured prior to running for all PMT's used in the calorimeter, and is parameterized as:

$$g_{PMT} = aV^{\alpha}, \tag{8}$$

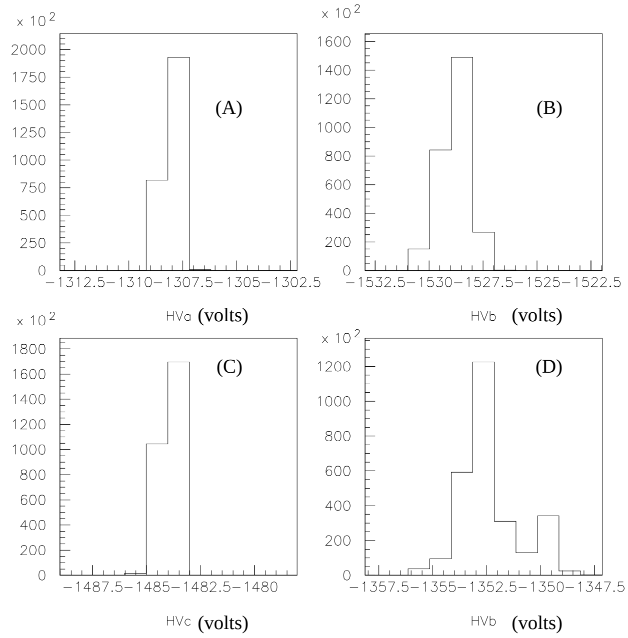

Figure 24: Typical HV readout values for four randomly selected PMT's. As one can observe, the HV readout does not vary more than 2-5 V.

where g_{PMT} is the gain of the given PMT, V is the HV in units of volts, and a and α are the fit parameters. The exponents α are determined for each PMT, and a typical value of α is ~ 6.8.

The NuTeV experiment implemented a slow monitoring system that monitored PMT HV values as described in Section 9.1. Six LeCroy 1440 HV mainframes supply high voltage to the calorimeter PMT's. The slow monitoring system read out 1 HV channel per second and completely cycled through all HV channels in 5 minutes. The entire record in the database is written to the neutrino data tape once every beam cycle as the last record in the given cycle. The readout resolution of the NuTeV HV slow monitoring system is $\sim$ 1 V; the PMT's are typically set at between -1400 V and -1500 V.

A study based on a total of 280,000 measurements of each individual HV read-back, taken over the entire run period, reveals that the typical variation of each PMT HV readout is within 2 V and the RMS of the distribution is typically less than 0.5 V. Figure 24 shows typical HV readout values of four randomly selected PMT's for all the readings throughout the entire run.

Despite the fact that we expect very small corrections due to HV variations based on the HV readout measurements, we correct for HV for the calibration beam due to the fact that calibration runs are typically localized in time while the gain correction factors are averaged over a longer time period.

HV corrections for each counter are done using the measured parameters in Eq. 8, relative to the counter gain correction factor at the center of the counter, averaged over the muon response map period. The relative gain correction factor is computed using Eq. 8 on an event-by-event basis and normalizing the gain at the given HV readout to that at the average HV readout of the PMT in the given run. The relative correction factor for counter i, f^i_{HV}, is defined as:

$$f^i_{HV} = \frac{\sum_{j=1}^{4} PH_{ij}(< V_{ij} > / V_{ij})^{\alpha_j}}{\sum_{j=1}^{4} PH_{ij}}, \qquad (9)$$

where $< V_{ij} >$ is the average HV readout value of PMT j of the counter i for the given run, V_{ij} is the HV readout for the given event, α_j is the exponent in Eq. 8 for PMT j, and PH_{ij} is the individual pulse height from the PMT j. As we expect, the typical overall size of this relative correction factor is on the order of 0.1% or less.

10 Measurement of Muon Energy Loss in the Calorimeter and Comparison with GEANT

The toroid spectrometer is located downstream of the 690-ton NuTeV calorimeter. For an accurate measurement of each muon's momentum, the energy lost by the muon in the calorimeter (ΔE) has to be included. A precise measurement of ΔE is also necessary for the calibration of the toroid using test beam muons. Knowledge of muon energy depositions is also needed for the hadronic energy measurement, since muons, originating in ν_μ charged current interactions, contribute to hadronic shower pulse heights.

A minimum-ionizing particle passing through the detector leaves a characteristic energy deposit in each of the scintillation counters. The energy loss of a muon traversing the calorimeter changes with energy. For high energy muons the contribution to the muon energy loss from bremsstrahlung, electron-positron pair production, and nuclear interactions increases. These processes may yield larger electromagnetic showers than would be true for a strictly "minimum-ionizing" particle. A coarse sampling calorimeter, such as NuTeV's, is strongly non-linear in energy between a fraction of an MeV to a few GeV. Hence the conversion of the light yield induced by a muon passing through the counters to measured muon energy loss in the calorimeter requires a differentiation between lower and higher energy processes. We use a GEANT-based simulation of the detector (McNuTeV) to determine the best pulse height to GeV conversion method or "reconstruction algorithm" for the total energy lost by the muon, ΔE. Tests of both the GEANT simulation and the reconstruction algorithm are described in the following sections.

Process	Value
Rayleigh Scattering	ON (IRAYL=1)
γ-Induced Fission	ON (PFIS=1)
δ-ray Generation above	DCUTE = 100 keV
Restricted Landau below	DCUTE = 100 keV
Direct Pair Production	ON (PPCUTM = 2.04 MeV)
Bremsstrahlung Tracking	(BCUTE = 100 keV)
	(BCUTM = 100 keV)
Other Particles	CUTGAM=100 keV
	CUTELE = 100 keV
	CUTNEU = 100 keV
	CUTHAD = 100 keV
	CUTMUO = 1 MeV

Table 5: Parameters with changed values from their default values in GEANT V3.215.

10.1 Counter Pulse Height Simulation using GEANT

The NuTeV calorimeter simulation segments the calorimeter into six identical carts, each of which consists of seven unit calorimeter layers described in Section 2. The steel, water, drift chamber gas, lucite, mylar, polythene, air, copper, and G10 are specified as separate GEANT volumes building the layers with sizes and configurations closely matching the physical detector. We find that very detailed modeling of the detector is necessary to achieve good agreement between calibration beam data and the GEANT simulation of muon responses.

We use version 3.215 of GEANT and set the physics control variables to their default values, with the exceptions listed in Table 5. The energy deposited in scintillation counters follows an avalanche in our 10-stage model of PMT's and is smeared statistically at each step. The number of photoelectrons used in the smearing is tuned to match the widths of muon dE/dx deposition in the data. Pedestals, gains, and the digitization of LOW and $HIGH$ channels of electronics are also simulated. Observed pulse heights, both for data and for the simulation, are expressed in units of MIP's, where 1 MIP is defined as a truncated mean of the energy loss of 77 GeV muon (see Section 6). The resulting GEANT events are passed through the same analysis chain as the actual data events.

10.2 Data/GEANT Comparisons for Muons

Muon calibration beam data are taken throughout the 1996-97 NuTeV run totaling approximately 250 10000-event data sets. Most of that data are 50 GeV muon sets used for measuring the magnetic field of the toroid. Another subset, also used in this study, consists of runs with muon energies spanning from 12.5 to 190 GeV. GEANT samples are generated with the energies, momenta, and

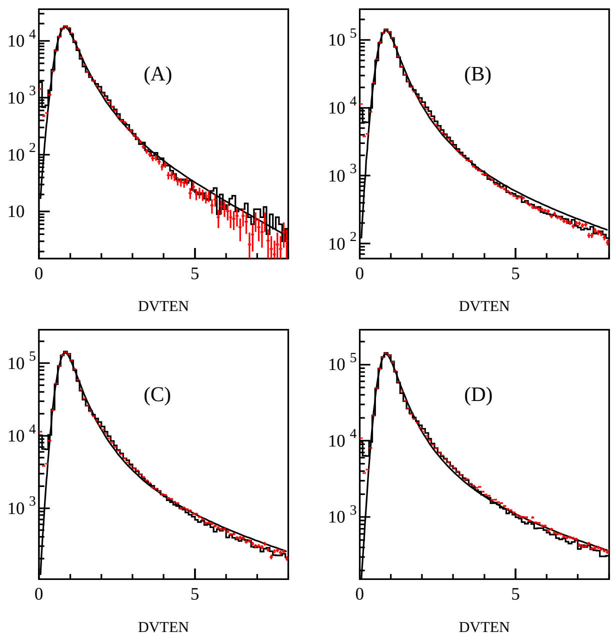

Figure 25: Counter response to muons in calibration beam (histogram) and Monte Carlo (crosses) for muon of energies of 15 (A), 50 (B), 100 (C), and 166 GeV (D). DVTEN (HIGH/LOW channel depending on saturation) are muon map corrected and measured in MIP's. All 84 counters contribute to the distributions. Solid lines represent 5-parameter asymmetric Gaussian fits (Eq. 10) to the distributions.

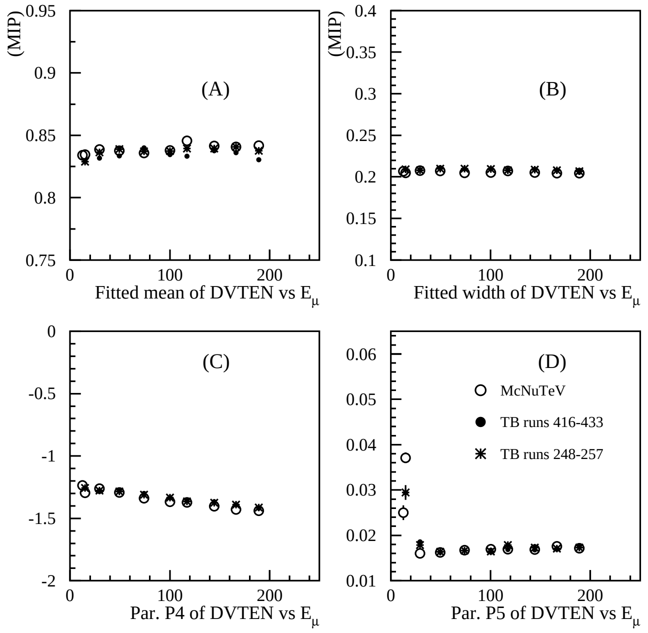

Figure 26: Fit parameters (A, B: mean and RMS of the Gaussian part, C and D: asymmetric tail, Eq. 10) to DVTEN distributions for Monte Carlo (open circles) and calibration beam muons plotted versus incident muon energy (E_μ).

positions at the entrance to the calorimeter matching the calibration beam data samples. In the comparisons, cuts are applied to the calibration beam muons to assure that the momentum measured in the test beam spectrometer and the x- and y-vertex positions are reconstructed within ± 3 standard deviations around the mean value.

Figure 25 illustrates the detector response to calibration beam data (histogram) for muons of energies of 15, 50, 100, and 166 GeV. The GEANT simulation is marked by crosses. DVTEN shown in the plots is the pulse height of a counter measured in units of MIP's, after application of the position dependent gain correction discussed in Section 6.1. It uses the *HIGH* channel of electronics until its ADC saturation (1900 ADC counts), and the *LOW* channel readout above that. The DVTEN distributions in muon energy bins are fitted with a five-parameter asymmetric Gaussian fit, $\mathcal{F}$, in which the width of the Gaussian runs on one side, varying with the x-axis:

$$\mathcal{F} = \frac{P_3 e^{-(x-P_2)^2/2\sigma^2}}{|P_1 \; P_3|} \tag{10}$$

$$\sigma = P_3 \max(1, (1-(P_4+xP_5)(x-P_2))) \tag{11}$$

Figure 26 gives the values of the four parameters of these fits (peak of the Gaussian portion of the distribution P_2, its width P_3, and, P_4 and P_5, two parameters describing the asymmetric tail) as a function of muon energy. The Monte Carlo is represented by open circles, while the muon data sets by solid circles and stars. The calibration beam data show that the most probable value of muon energy loss in a counter is independent of muon energy in the 20-200 GeV range (see Figure 26). This is to be contrasted with almost linear increase with muon energy of the mean energy loss in the counter (also Figure 29). Figure 27 shows the pulse heights summed over 84 counters traversed by muons (DVTEN SUM distributions). This summed plot would magnify small discrepancies (e.g., in the tails) in comparison of calibration data and the Monte Carlo, but GEANT still describes the data well. A summary plot containing fit parameters to DVTEN SUM histograms for all available muon energy points is shown in Figure 28. The mean and RMS values (not from fits, but from the histogram statistics) for the DVTEN and DVTEN SUM distributions are plotted in Figure 29. From these calibration beam data-GEANT comparisons, we conclude that both the low and high energy components of the muon energy loss in the calorimeter are well modeled in our Monte Carlo over the full scale of such depositions. Modeling of GEANT muon energy loss in the steel and remaining absorber materials can be checked using so-called range-out muons. Those are low energy calibration beam muons that stop in the calorimeter. Our measurements give the mean length of

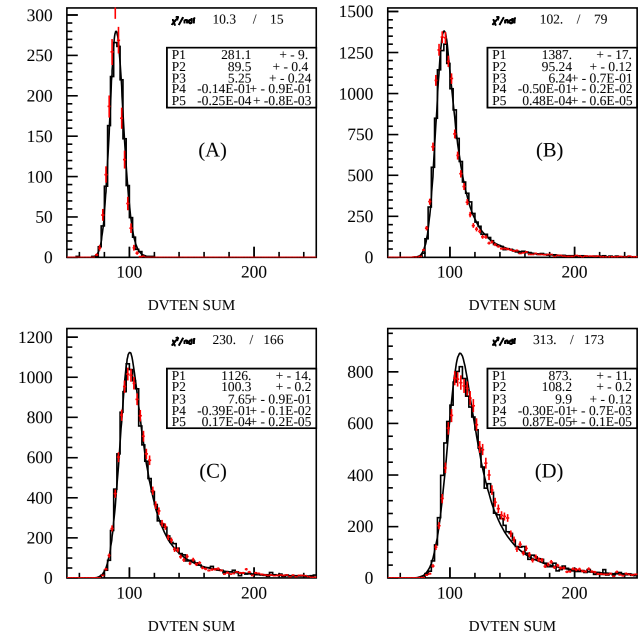

Figure 27: Counter response to muons summed over 84 counters in calibration beam (histogram) and Monte Carlo (crosses) for muon of energies of 15 (A), 50 (B), 100 (C), and 166 GeV (D).

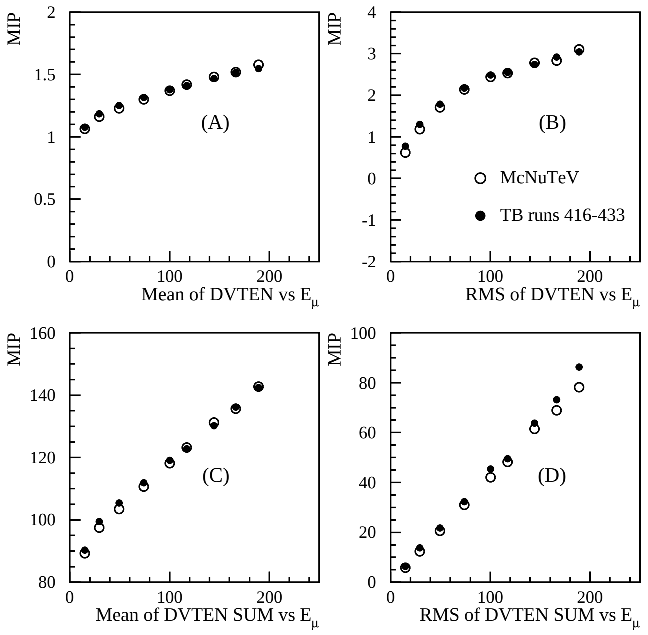

Figure 29: Mean values of DVTEN (A) and DVTEN SUM over 84 counters (C) distributions for Monte Carlo (open circles) and calibration beam muons (solid circles) as well as RMS values of these distributions.

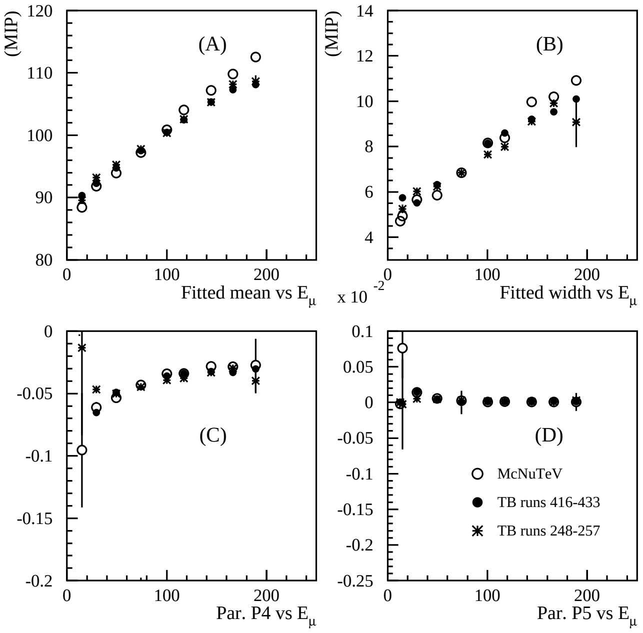

Figure 28: Fit parameters (A, B: mean and RMS of the Gaussian part, C and D: asymmetric tail, Eq. 10) to DVTEN SUM distributions for Monte Carlo (open circles) and calibration beam muons plotted versus incident muon energy (E_μ). DVTEN SUM is the sum of the DVTEN over 84 counters.

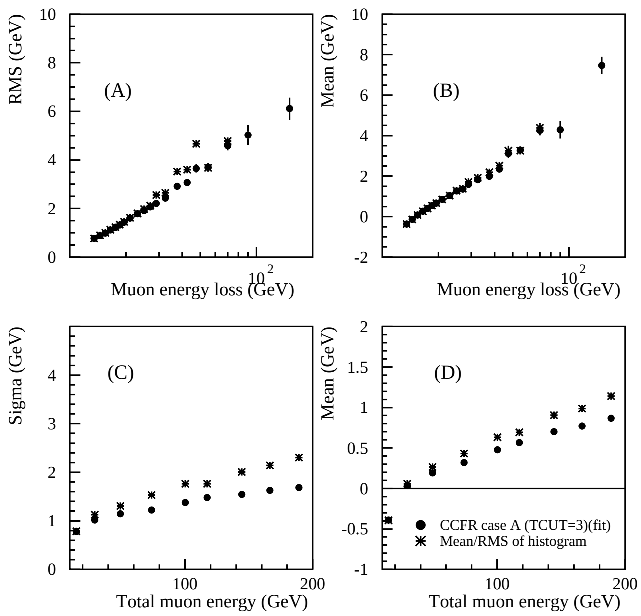

Figure 30: Method α: The width (A) and mean (B) from Gaussian fit (solid circle) and histogram statistics (stars) of the difference between "true" ΔE and reconstructed ΔE distributions in muon energy loss bins. C and D: the same in muon momentum bins.

75.7±0.3 counters for a 12.5 GeV muon in the data versus 74.7±0.09 in the simulation. The agreement between data and Monte Carlo in the mean length is only within about three standard deviations. One possible cause of this disagreement is the lack of any correlated counter noise in the Monte Carlo.

10.3 Study of Muon Energy Loss Reconstruction Algorithm Using GEANT

The goal of this study is to find an optimal algorithm to determine the muon energy loss in the calorimeter, ΔE, from the observed muon pulse height. We reconstruct ΔE and compare it to the "true" ΔE known from GEANT on an event-by-event basis in the range of 15–190 GeV. We define TCUT as the counter pulse height at which we switch from applying C_μ ("low energy") to C_e ("high energy") conversion from MIP's to GeV, under the assumption that sufficiently high pulse heights arise from electromagnetic processes sampled over several counters. Three different reconstruction schemes for ΔE are studied:

Method α: A model of two conversion constants C_μ and C_e and TCUT of 3 MIP's (this is a scheme used in our predecessor experiment CCFR, where C_e is determined from electron calibration beam data).

Method β: A "one-function model", where one function $C_\mu(E_\mu)$ is used to account for ionization and the increase of the radiative component of dE/dx with energy.

Method γ: A model of conversion function $C_\mu(E_\mu)$ varying with muon energy E_μ, applied below TCUT of 5 MIP's, and a constant conversion C_e above that TCUT.

As an illustration, we show the widths and the means of the difference between the "true" and reconstructed ΔE distributions in either muon energy bins or in the bins of the muon true energy loss for Method α in Figure 30 and Method γ in Figure 31. Both the fitted mean and sigmas of Gaussian fits to these distributions (solid circles) and the average values and RMS (stars) of these distributions are plotted. Notice that Method α underestimates ΔE for high energy electromagnetic depositions if the lower end of the energy loss spectrum is set to match GEANT's "true" ΔE (Figure 30(B)). Similarly for Method β (not shown) – no $C_\mu(E_\mu)$ can be found that describes the conversion from MIP's to GeV for both the most probable and the mean dE/dx at the low and high ends of muon energy spectrum at the same time. In Method γ, where the variation in low-energy radiative depositions with muon energy is accounted for by variation of

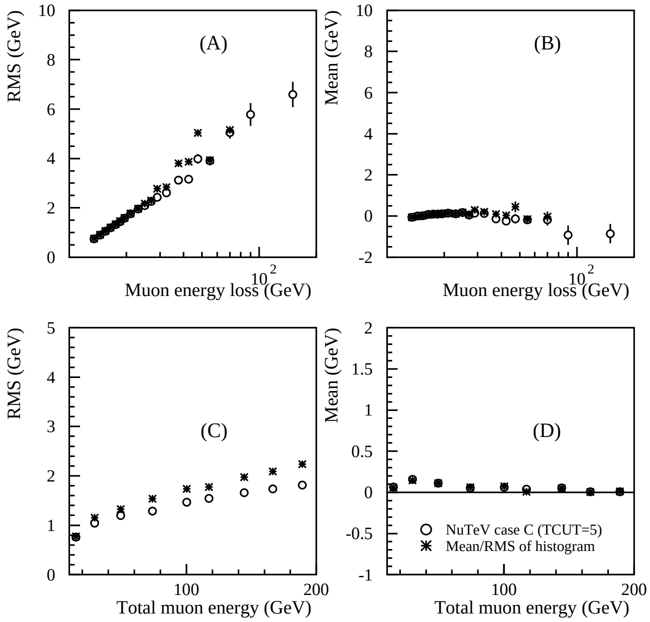

Figure 31: Method γ. The fitted widths (A) and means (B) of the difference between true ΔE and reconstructed ΔE distributions in muon energy loss bins. (C, D): the same in muon momentum bins.

the conversion function $C_\mu(E_\mu)$, we find the best match of the "true" ΔE for all muon energies and ΔE values (Figure 31). The function $C_\mu(E_\mu)$, based on the best calibration beam-to-GEANT match, is shown in Figure 32.

Figure 33 illustrates the total muon energy loss over the length of NuTeV calorimeter in terms of mean and the most probable value, where the latter is defined as the result of a fit of asymmetric Gaussian function $\mathcal{F}$ (parameter P2) to the ΔE distribution. Figure 34 gives a ratio of the most probable ΔE for 50 GeV calibration beam muons, traversing the NuTeV calorimeter at different angles and transverse positions, to a nominal 15.2 GeV GEANT prediction for their energy loss. The ratio is plotted as a function of muon azimuthal angle, ϕ, at the most upstream surface of the detector. As can be seen in this figure, we reconstruct muon ΔE to within ±0.7%, independent of ϕ (or position in the counter). This is an important verification of the muon map correction and counter gain stability over time. The counter pulse heights for these calibration beam muon samples are corrected by gains that vary by as much as an order of magnitude, depending on their transverse vertex and pathway through the calorimeter.

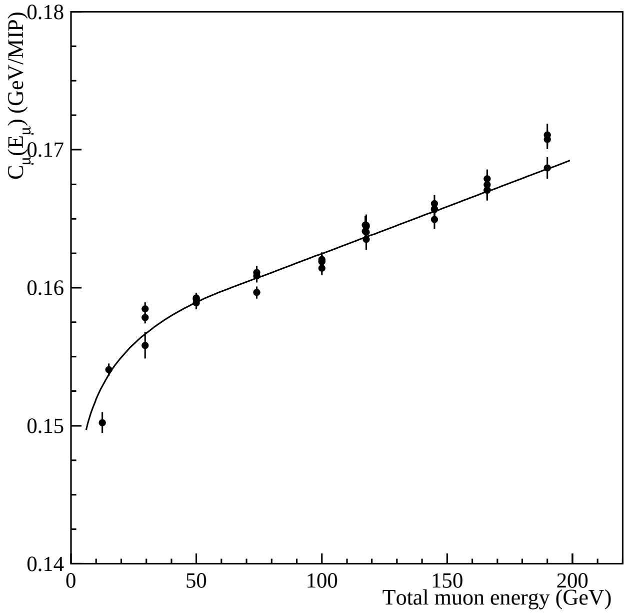

Figure 32: Energy dependence of calibration beam muon depositions of pulse heights below 5 MIP's, over 84 counters, shown in units of GeV/MIP and the parameterization $C_\mu(E_\mu)$.

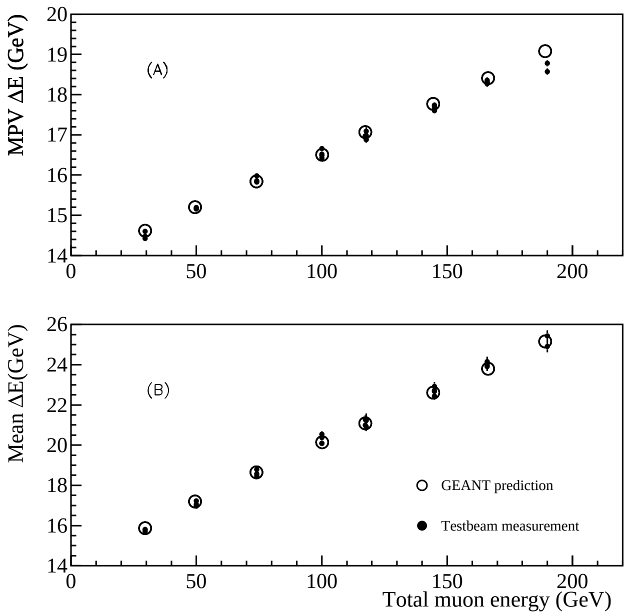

Figure 33: Most probable (A) and mean value (B) of total muon energy loss in NuTeV calorimeter. Comparison of GEANT prediction (open circle) and calibration beam measurement (solid circles) versus muon energy.

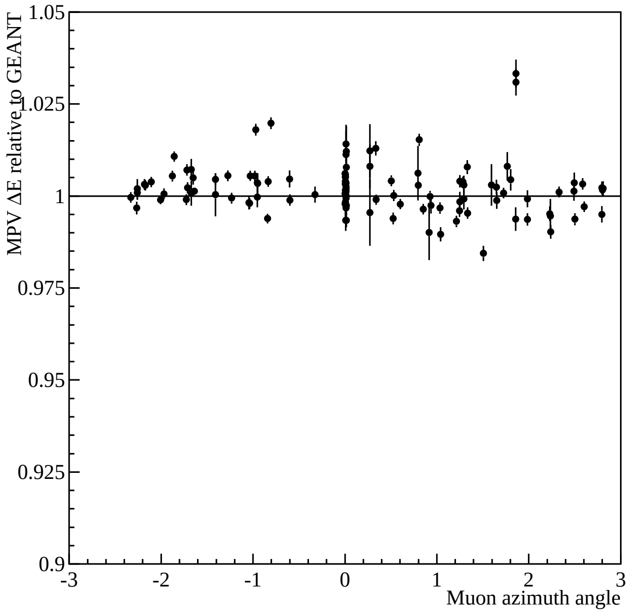

Figure 34: Ratio of the most probable values of ΔE for 50 GeV calibration beam muons to GEANT prediction (15.2 GeV) as a function of muon azimuthal angle.

11 Shower Energy Definition

The definition of the shower energy used in the hadron energy calibration is:

$$E_{shower} = C_\pi \left[\sum_{i=1}^{place} PH_i + \sum_{i=place}^{place+19} h_i PH_i \right], \quad (12)$$

where i is the counter number; PH_i is the pulse height normalized for the muon gain as described in Section 6 in units of MIP in counter i; h_i is the hadron/muon gain ratio (described in Section 7); and C_π is the hadron calibration constant. The variable *place* is the counter where the hadron shower started to develop, and is determined by an algorithm designed to locate where a neutrino interaction begins. *place* is defined as the upstream of two consecutive counters which have more than a certain number of MIP's, where that number depends on the total energy of the hadron shower and is at least four. Upstream of *place* the hadron is treated as a minimum ionizing particle. In contrast, electron showers always start at the first counter. For the electron energy measurements described later only the seven most upstream counters are used, and the hadron/muon gain ratio is applied to each counter's pulse height.

In order to determine the hadron energy calibration constant which, in our definition, is the GeV-to-MIP con-

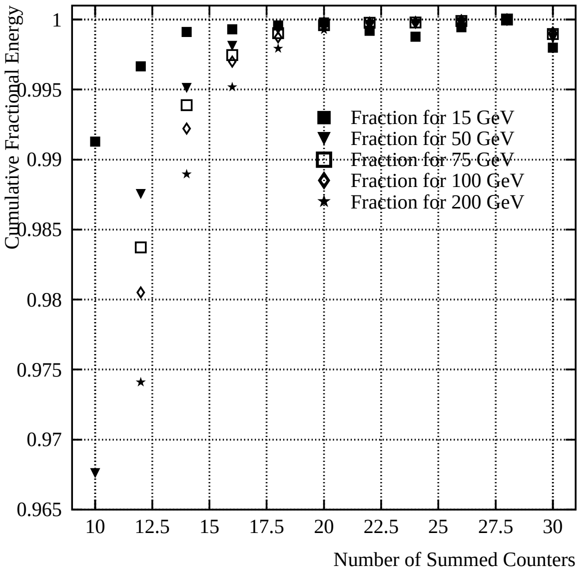

Figure 35: Cumulative fractional shower energy as a function of the added number of counters. Note that for all energies, adding 20 counters provides full longitudinal shower containment.

version factor (C_π), it is important to define the energy variable to contain the entire shower. On the contrary, for a precision measurement, one does not want to include too many counters in the sum because adding more counters than necessary would introduce noise into the system due to pedestal fluctuations in the counters. Finally, the algorithm should be as close as possible to that used in analyzing the neutrino data, which also sums over a certain number of counters following *place*. We perform a study to optimize the number of counters over which to sum the pulse heights. Using hadron beams over the energy range between 10 GeV and 190 GeV, we determine that summing over 20 counters beginning from the most upstream counter is optimal for calibration purposes.

Figure 35 shows the cumulative fractional energy as a function of the number of summed counters for various hadron beam energies. Since we summed the pulse heights of at least 20 counters dependent on the measured hadron energy, we introduce an energy dependent noise level. This noise level depends on beam energy because the shower penetration depth depends on beam energy. The number of counters without actual shower energy increases with decreasing beam energy and the noise level gets more prominent for low energy beams. Therefore, the low energy calibration has a larger contribution from this noise effect. However, since hadronic energy resolution is worse at low energies, this noise is less important.

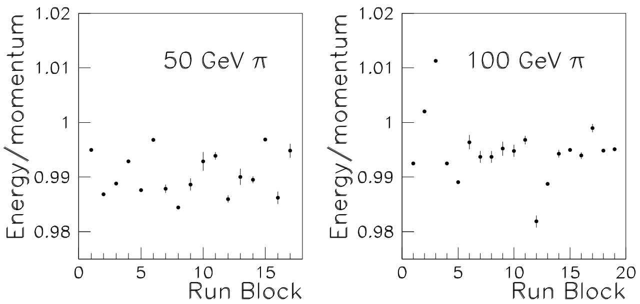

Figure 36: Remaining time dependence of the ratio of reconstructed calorimeter energy divided by measured beam momentum. The left graph is for 50 GeV runs, and the right is for 100 GeV runs. The horizontal axis is time in units of blocks, where each run block corresponds to a period of about 2 weeks. The responses are obtained after all the time-dependent corrections are applied to the data, but before the final energy scale is set.

12 Hadron Energy Response and Resolution

The simplest test of the muon calibration technique described above is the time dependence of a particular calibration beam setting. Figure 36 shows the time dependence of both 50 GeV hadron and 100 GeV hadron runs that are taken periodically during the course of the experiment. The RMS of the ratio between reconstructed calorimeter energy and beam momentum is 0.4-0.5%, and is due to the statistical uncertainty in the muon maps themselves, as well as the electronics gain coefficients.

The calorimeter response to a monochromatic beam of hadrons can be characterized by a function similar to a Poisson distribution. This is because the energy reconstructed by the calorimeter is proportional to the number of shower particles produced by the incident hadron. The statistical fluctuation of the number of electromagnetic particles in the shower causes the response to look Poisson-like at low energies, and to become Gaussian at high energies. This can be seen in figure 37, where the 5 GeV data are much less symmetric than the 190 GeV data around the peak of the Energy/momentum distribution. Figure 38 shows that the Poisson-like function, defined below, describes the data over several decades. Fluctuations in where the primary hadron interaction occurs can also contribute to the asymmetric shape of this distribution, but again these fluctuations have a negligible effect at high energies.

The Poisson distribution is normally written as

$$P(N,\mu) = \frac{\mu^N e^{-N}}{N!}, \tag{13}$$

where $P(N,\mu)$ is the probability of seeing N shower particles if μ are expected. The RMS of this distribution is $\sqrt{\mu}$ and the mean is μ. As N gets large this approaches a simple Gaussian distribution. To remove any effects from

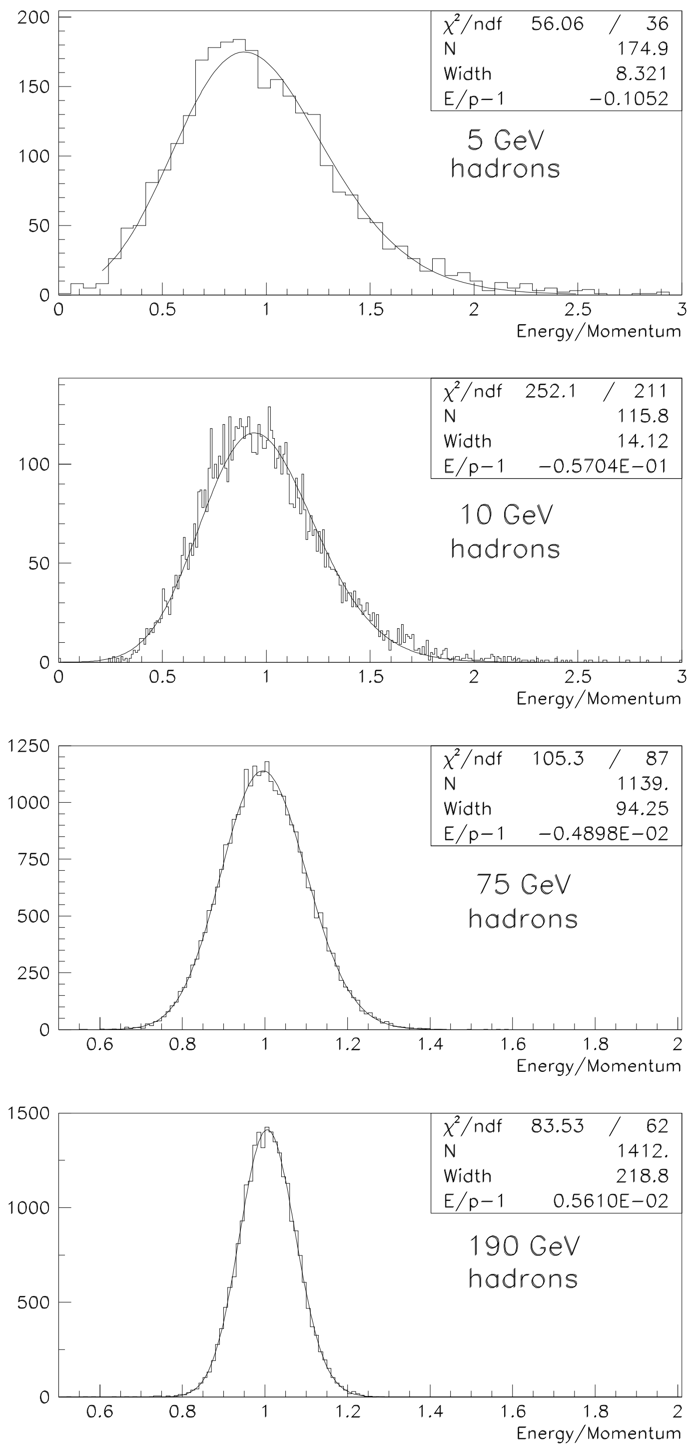

Figure 37: Poisson fits to the calorimeter energy divided by momentum distributions for four different energies: 5 GeV, 10 GeV, 75 GeV, and 190 GeV.

variations in time of the calibration beam momentum, the calorimeter energy is divided by the reconstructed particle momentum on an event-by-event basis. This implies that the mean of the distribution is decoupled from the width, but the fractional width (width divided by the mean) remains $1/\sqrt{\mu}$. Generalizing Eq. 13 to decouple the mean from the width and expanding about the peak, we can parameterize the Poisson distribution as follows (note that keeping only the first term in $F(x)$ gives a Gaussian distribution):

$$P(x) = Ae^{-F(x)}, \tag{14}$$

where

$$x = B(E/p - C), \tag{15}$$

and

$$\begin{aligned} F(x) = {} & \frac{1}{2}\left(B - \frac{1}{2} + \frac{1}{24B}\right)\left(\frac{x}{B} - 1\right)^2 \\ & + \frac{1}{6}\left(B - \frac{1}{4} + \frac{1}{72B}\right)\left(\frac{x}{B} - 1\right)^3 \\ & - \frac{1}{48}\left(B - \frac{1}{6}\right)\left(\frac{x}{B} - 1\right)^4, \end{aligned} \tag{16}$$

where E is the measured hadron energy, p is the reconstructed calibration beam momentum, the peak $E/p-1$ of the distribution is C, and the width of the distribution is B. The fractional width of the distribution is $1/\sqrt{B}$. At beam momenta of 30 GeV and above, this equation is very close to a Gaussian distribution. Figure 37 shows fits to the above equation for four different energies.

The energy dependencies of the mean E/p distribution and the Poisson widths are shown in Figure 39. If the hadron calibration constant C_π, as defined in Section 11, is set to 0.212 after all corrections, the mean energy response divided by the reconstructed test beam momentum at 75 GeV is 1.000±0.001. Note that the non-linearity of the calorimeter between 10 GeV and 190 GeV is only 3%. This comes from the fact that electrons and

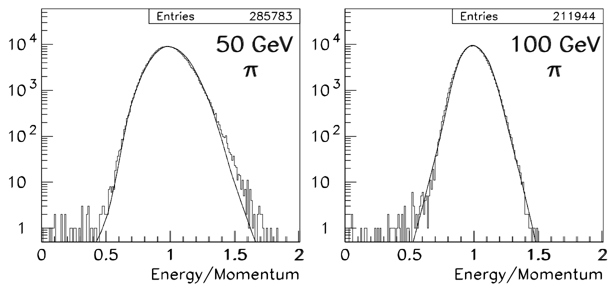

Figure 38: The distributions of calorimeter responses to 50 and 100 GeV hadrons with very high statistics. The data follow the Poisson-like shape over several decades.

hadrons have a very similar response, and so the electromagnetic component of the shower, which changes as a function of energy, will not change the reconstructed energy. The Poisson widths can be fitted to the standard form $\sigma(E)/E = A \oplus \frac{B}{\sqrt{E}} \oplus \frac{C}{E}$, where A is a constant term coming from calibration uncertainties, B is the stochastic term from the sampling of the shower, and C is from noise due to pedestal fluctuations. The data show no evidence for a noise term and so C is removed from the fit. The stochastic term is proportional to the square of the thickness of the sampling layer.

The energy points below 10 GeV have to be measured using a different energy algorithm, since the one that is designed for neutrino interactions (requiring at least 4 MIP's in two consecutive counters) is biased for hadron showers below 10 GeV. For these lowest points,

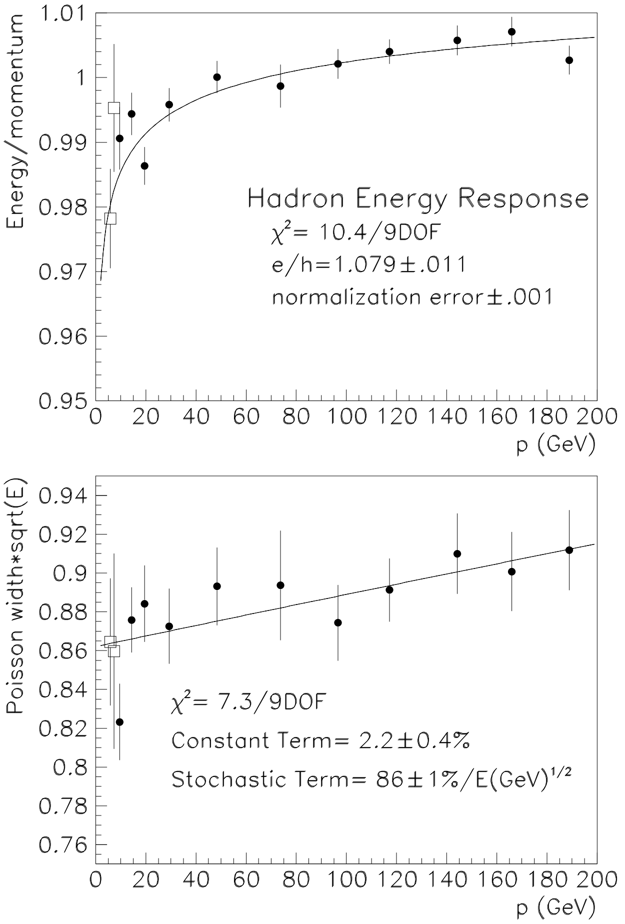

Figure 39: Hadron energy response versus reconstructed test beam momentum and comparison with fit to Groom's parameterization for non-linearity, and Poisson width distribution versus energy with fit to $\sigma(E)/E = A \oplus \frac{B}{\sqrt{E}}$. The open symbols are lower energy runs with slightly different cuts and are not used in the fits.

the energy is determined simply by summing the most upstream twenty counters, and is using the hadron gain

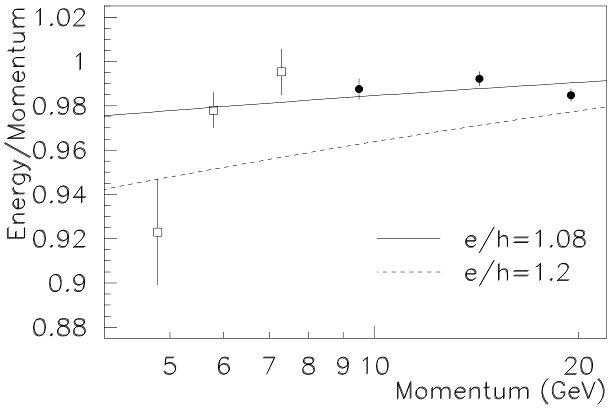

Figure 40: Lowest energy hadron response versus reconstructed test beam momentum and comparison with fit to Groom's parameterization for non-linearity. The open symbols are lower energy runs with slightly different cuts.

coefficients for each counter. To remove electrons from the low energy samples, cuts are made based on Čerenkov counter particle identification system in the beamline. To remove muons in the hadron beam, a loose cut is made on the most upstream of three consecutive counters that have less than 0.25 MIP's in them. The latter cut removes events caused by muons in the hadron beam, but did not remove events with secondary muons created in the hadron shower. Finally, because the lowest energy points have low statistics the means of the energy/momentum distributions are plotted rather than the results of the Poisson fits. Figure 40 shows the nonlinearity of the NuTeV calorimeter to low energy hadrons. For energies 5.9 GeV and above, Groom's parameterization (see section 13) with $e/h = 1.08$ (solid line) agrees well with the data. The overall agreement with the parameterization is not improved by changing e/h from 1.08 in the hadron response curve, as is also shown in figure 40.

Finally, any additional position dependence not taken into account in the muon map procedure outlined earlier is studied using a 75 GeV hadron beam aimed at different locations on the front face of the calorimeter using the rotating dipole at the end of the momentum analyzing magnet chain in the spectrometer. For hadron showers that start more than 50 cm from the closest edge of the detector, the energy reconstruction is constant to better than a 0.5% in the calorimeter response, when normalized using the muon maps. By aiming the hadron beam as close to the edges as is safe, it is determined that hadron shower leakage does not begin to affect energy reconstruction until the shower starts at 25 cm from the calorimeter edge.

Table 6 lists systematic errors that contribute to the uncertainty in overall hadron energy scale of the calorimeter. It is clear from the list that the largest single systematic error is due to the statistical uncertainty in the hadron/muon gain ratio for the counters.

Source	Fractional Uncertainty
Hall Probe Readout (from shunt comparisons, see Figure 22)	0.03%
Magnetic Field Homogeneity (from Position-dependence measurements)	0.03%
Beam Composition Corrections (100% of effect above 30 GeV)	0.03%
Transition Effect Uncertainties (10% of effect on hadrons)	0.03%
Temperature Corrections (10% of effect)	0.02%
High Voltage Correction	< 0.01%
Spectrometer Alignment	0.1%
Uncertainty in hadron/muon gain ratios	0.4%
Fit Normalization Error	0.1%
Statistical	< 0.01%
Total	0.43%

Table 6: Table of contributions to uncertainty in overall hadron energy scale.

13 Hadron Response Comparison to Monte Carlo

The task of reproducing the calorimeter attributes in a GEANT-based Monte Carlo is a challenging one. This is demonstrated in Figure 39. Both the non-linearity and hadron energy resolution of the calorimeter depend critically on the difference in the calorimeter's response to hadrons and to electrons (e/π). In order for a Monte Carlo to simulate hadrons correctly, it must first correctly simulate the calorimeter's electron response, and then have an accurate hadron shower model, a thorough description of the geometry of the calorimeter, and an accurate model for the way particles propagate in the particular media that comprise the calorimeter. Section 14 describes the calorimeter electron energy response and the resolution in detail; the studies show that the electron energy resolution is well-modeled in the detailed GEANT simulation of the calorimeter.

Once the electron to hadron response is measured in the data at a particular energy, one can minimize the dependence on hadron shower generators by only using them to predict the fraction of π^0's produced in a hadron shower as a function of energy, $f_{\pi^0}(E)$. Figure 41 shows three different hadron generators' predictions for the fraction of electromagnetic energy deposited in a hadronic shower as a function of energy. Two parameterizations for this fraction are also shown; Wigmans' parameterization [22] is $f_{\pi^0} = 0.11\ln(E)$ and Groom's is $f_{\pi^0} = 1 - (\frac{E}{0.96\text{ GeV}})^{-0.184}$.

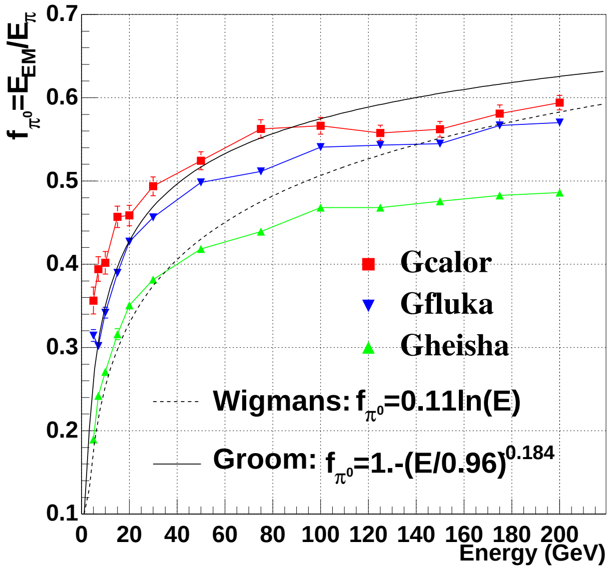

Figure 41: Fraction of electromagnetic energy in a hadronic shower as a function of hadron energy for three different hadron shower generators: GHEISHA, GFLUKA, and GCALOR. Fits of the simulation to both the Wigmans' [22] and Groom's [17] parameterizations are also shown.

The reconstructed energy of a shower is defined as

$$E = E_{true}(h(1 - f_{\pi^0}(E)) + e f_{\pi^0}(E)), \qquad (17)$$

where h is the ratio of reconstructed to true energy for a "pure" hadron, and e is that same ratio for a "pure" electron. The non-linearity as a function of energy can be expressed as the ratio of $R(E)/R(E_{ref})$, where $R(E) = E/E_{true}$. In other words,

$$\mathrm{non-linearity} = \frac{1-f_{\pi^0}(E)+\frac{e}{h}f_{\pi^0}(E)}{1-f_{\pi^0}(E_{ref})+\frac{e}{h}f_{\pi^0}(E_{ref})}. \qquad (18)$$

By requiring the three generators shown in Figure 41 to have the same $R(E)/R(E_{ref})$ at 50 GeV, one can construct the expected non-linearity as a function of energy. This is shown in Figure 42. Although the fraction of electromagnetic energy at a given energy varies among the different generators, the predicted non-linearity is similar.

By fitting the hadron energy response shown in Figure 39, assuming the non-linearity predicted by Groom's parameterization, one arrives at a value of $\frac{e}{h}$ of 1.079 ± 0.011. Given that at 75 GeV the fraction of π^0's is roughly 50%, $\frac{e}{\pi} - 1 = 0.5(\frac{e}{h} - 1)$. Therefore, the electron to hadron response ratio is roughly of 1.035 ± 0.01 at 75 GeV. This is in agreement with what is seen in

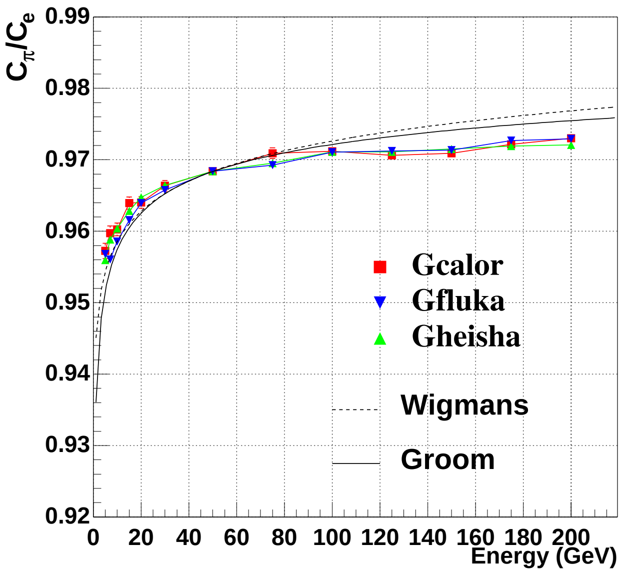

Figure 42: Predicted non-linearity for three different hadron shower generators: GHEISHA, GFLUKA, and GCALOR, where all three are required to have the same value of $E/E(true)$ at 50 GeV. The prediction for both the Wigmans and Groom parameterizations are also shown.

the calibration beam comparisons between hadrons and electrons, as will be described in Section 14. A similar conclusion has been reported by the CDF collaboration [23] for their plug-upgrade hadron calorimeter, which has a much larger non-linearity.

As a side note, if we use the different hadron shower generators to predict the ratio of electron to hadron response at 75 GeV, they all give different ratios. Since the difference between these responses is also a large factor in determining the hadron energy resolution, they all predict correspondingly different hadron energy resolutions (the closer the electron to hadron response ratio is to unity, the better the hadron energy resolution).

GFLUKA [19] predicts the lowest ratio of electron to hadron response, and also predicts a hadron energy resolution of $0.80/\sqrt{E(GeV)}$. GHEISHA [18] predicts a ratio of electron to hadron response of 1.15 at 75 GeV rather than 1.09, and predicts a hadron energy resolution of $1.15/\sqrt{E(GeV)}$. Finally, GCALOR [20] predicts that the ratio of electron to hadron response is less than unity, rather than greater than unity.

All three generators are tested using identical GEANT energy cutoff settings and identical geometry input. Although GHEISHA is native to the GEANT program, GFLUKA and GCALOR are imperfect implementations of the original FLUKA and CALOR programs and have been known to produce somewhat different results than the original generators [21].

Finally, although the hadron non-linearity is now parameterized and well-measured, the purpose of the NuTeV calorimeter is to measure hadron showers generated by neutrino interactions, not hadron showers generated by a single charged hadron. To study any possible difference the LUND Monte Carlo program is used to determine the first set of particles produced from the hadron shower of a neutrino interaction. Groom's parameterization is then used to calculate the electromagnetic fraction of the charged hadrons which get produced. Although the charged hadrons have lower energy than the initial total hadron energy, and as such would have a lower electromagnetic fraction, there are also neutral pions that are produced, which increase the electromagnetic fraction. The two effects cancel, keeping the electromagnetic fraction as a function of total hadron energy the same between neutrino-induced hadrons and single hadrons, to a few per cent. The resulting effect on the neutrino-generated hadron non-linearity is negligible compared to the statistical error on the e/h fraction itself, and the overall energy scale change is consistent with zero to better than 0.1%.

14 Electron Energy Response and Resolution

The calorimeter response to electrons can be measured using the calibration beam when set to the electron mode, as described in Section 8.2. Although there is a large contamination of muons in the electron running, this is easily removed from the data sample by looking at the most downstream counter and by selecting events with more than one minimum ionizing particle in them. Since electrons penetrate no more than a few cm of steel, most of the energy is deposited in the first three counters, so calibrating the detector response to electrons is extremely dependent on the muon maps of those three counters, and has larger systematic uncertainties due to statistical errors in the muon maps.

Figure 43 shows the shape of the electron energy de-

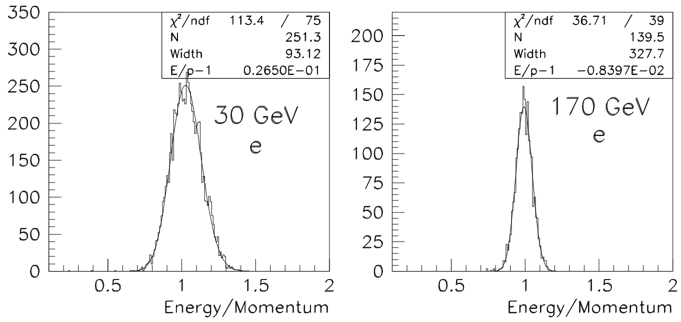

Figure 43: Calorimeter energy divided by test beam reconstructed momentum distributions for 30 GeV and 170 GeV electrons, and the results from the Poisson fit to the distribution.

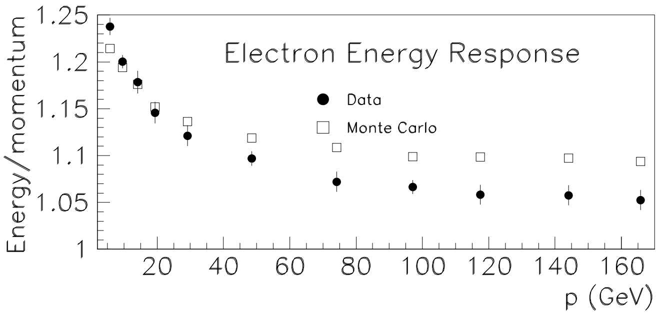

Figure 44: Normalized response of calorimeter to electrons as a function of energy for both data (solid circles) and GEANT-based Monte Carlo (open squares).

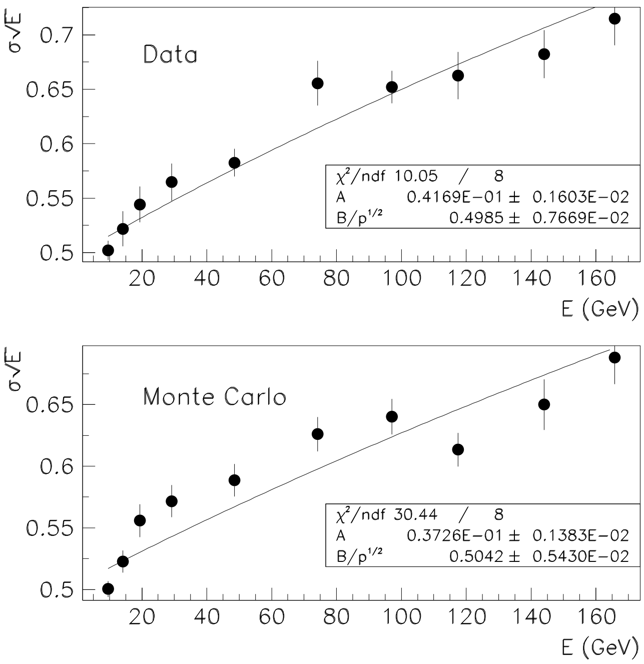

Figure 45: Electron energy resolution for both data and GEANT-based Monte Carlo as a function of energy, and the results to a fit of the form $\sigma(E)/E = A \oplus \frac{B}{\sqrt{E}}$.

position for 30 and 170 GeV electrons, as well as the fit to the Poisson distribution. The detailed GEANT simulation reproduces the shapes of the distributions well, but there are substantial differences between the mean values as a function of energy.

Figure 44 shows the electron energy divided by momentum for both data and Monte Carlo. There are several contributions to the large non-linearity. The most important contribution to the non-linearity, and the only one present in the GEANT simulation, is due to the fact that electrons arrive at the upstream edge of the calorimeter and begin showering immediately. If one generates the electron showers in the simulation equally distributed throughout the steel, as neutrino interactions (and hadrons to first order) would be, the GEANT response is linear to better than 0.5%.

There are two other effects that are present in the data but not in the simulation, and these give rise to the additional non-linearity that is seen in the data. The electron response depends critically on the both the muon gain and the hadron/muon gain ratio for the first two counters. These ratios are only known to about one per cent, per counter, so this contributes an additional uncertainty which could affect both the scale and the non-linearity. Another contribution to the non-linearity is due to the fact that there are cuts on the reconstructed track momentum in the data that cannot be made in the Monte Carlo simulation. These cuts do not affect the hadron response because hadrons are extremely unlikely to shower before the calorimeter. There is however approximately one radiation length of material distributed throughout the last arm of the calibration beam spectrometer. This material is included in the GEANT simulation, but its effect on the tracking efficiency is not. This is particularly important at high energies, where the upstream showers are most likely to cause ambiguities in the momentum determination.

One correction to the gains of the first few counters in the detector that is extremely important for measuring the electron response of the calorimeter, is due to the RE effect which is discussed in Section 9.3.

The GEANT-based Monte Carlo predicts the sampling term in the resolution of electron energies to within 2%, as can be seen in Figure 45. As with the hadron resolution, the electron resolution can be fit to the form $\sigma(E)/E = A \oplus \frac{B}{\sqrt{E}} \oplus \frac{C}{E}$, and the noise term ($C$) is consistent with zero for both the data and Monte Carlo and is removed from the fit. The sampling term B for electrons is $0.499 \pm 0.008(\sqrt{\mathrm{GeV}})$ from data while it is $0.504 \pm 0.006(\sqrt{\mathrm{GeV}})$ in Monte Carlo, showing extremely good agreement.

Finally, a very important parameter of the calorimeter is the difference between electron and hadron responses as a function of energy. Section 13 describes how the hadron resolution and non-linearity depend critically on this difference. In other words, the more similar the electron and hadron responses are, the better the calorimeter resolution, and the more linear. The measured electron/hadron difference must be corrected by 1% to account for the fact that the electrons in the calibration beam started upstream, while those from neutrino interactions (or those from hadron showers) are much more uniformly distributed throughout each steel plate. The ratio of the reconstructed energy of electrons compared to that of hadrons is 1.06 ± 0.03 at 75 GeV, which corresponds to a small non-linearity, in agreement with what is seen in the calorimeter response as a function of energy.

15 Conclusions

In this paper we outline the calibration technique and subsequent testing of the NuTeV calorimeter. The overall gain and time dependence of the calorimeter are tracked using muons from the neutrino beam, and PMT gains are determined to better than one percent for a given run period. Using several sets of linear ADC's with different gains, we are able to cover the large dynamic range required to reconstruct minimum energy deposition at the percent level, as well as reconstruct energy deposition from 600 GeV neutrino induced hadron showers.

Although the technique of calibrating the detector with muons from neutrino interactions may seem simple and straightforward, checking this technique requires a very detailed and well-designed calibration beam. By using a low mass spectrometer with long lever arm, NuTeV is able to achieve event-by-event momentum resolution of better than 0.1%. In addition, as a consequence of careful calibration of the magnets in the spectrometer and measurement of the particle composition of the hadron beam, the absolute hadron energy scale of the calorimeter is determined to better than 0.3%.

The non-linearity in the hadron response of the calorimeter is measured and agrees with predictions based on the measured difference between the hadron and electron response at a particular energy. Finally, the muon and electron responses of the calorimeter are shown to agree with a GEANT-based Monte Carlo prediction, once the details of the calorimeter geometry are accurately included. The vital statistics of the NuTeV calorimeter are summarized in Table 7. In conclusion, NuTeV has accomplished its goal of calibrating the absolute energy scale of its calorimeter to the level dictated by the physics analyses that NuTeV is performing. The calibration beam data also yields a wealth of information about hadron, electron, and muon interactions in an iron-scintillator sampling calorimeter. These can be used to study designs of future calorimeters with similar geometries, such as the MINOS detector to search for neutrino oscillations, as well as for space-based calorimeters to measure cosmic ray fluxes [24].

Table 7: Vital statistics of the NuTeV calorimeter.

Redeeming Feature	Measurement
Hadron Non-linearity from 5.9 GeV to 190 GeV	$3.0 \pm 0.5\%$
Hadron Energy Scale Uncertainty	0.43%
Hadron Energy Resolution: $\sigma(E)/E = A \oplus \frac{B}{\sqrt{E}}$ A: Constant Term B: Stochastic Term ($\sqrt{GeV}$)	 0.022 ± 0.001 0.86 ± 0.01
Residual position dependence of hadron energy reconstruction more than 50 cm from edge	$< 0.5\%$
Electron/Hadron Response Ratio (using Groom Parameterization)	1.08 ± 0.01
Electron Energy Resolution: A: Constant Term B: Stochastic Term ($\sqrt{GeV}$)	 0.042 ± 0.002 0.499 ± 0.008
Average Number of Photoelectrons/counter/MIP	30
Hadron MIP-to-GeV Conversion Factor (C_π GeV/MIP)	$.212 \pm .001$

Acknowledgements

We would like to express our gratitude to the US Department of Energy and the US National Science Foundation for their support. We express our deep appreciation to Fermilab for providing all the necessary technical support in this experiment. We thank the numerous people at Fermilab and the collaborating institutions who helped in all the facets of this project. At Fermilab, we especially appreciate the help of the Beams Division, as well as the Engineering, Mechanical, Electrical, and Survey and Alignment groups.

References

1. R.H.Bernstein *et al.*, NuTeV Collaboration, "Technical Memorandum: Sign Selected Quadrupole Train," FERMILAB-TM-1884 (1994); J.Yu *et al.*, NuTeV Collaboration, "Technical Memorandum: NuTeV SSQT performance," FERMILAB-TM-2040 (1998).
2. CCFR Collaboration, W. Sakumoto *et al.*, Nucl. Instrum. Methods, **A294** (1990) 179; B.J. King *et al.*, Nucl. Instrum. Methods, **A302** (1990) 179.
3. K.S. McFarland *et al.*, CCFR/NuTeV Collaboration, Eur.Phys.J. **C1**, 3/1, 509 (1998).
4. W.G. Seligman *et al.*, CCFR/NuTeV Collaboration, Phys.Rev.Lett. **79**, 1778 (1997).
5. Fermilab Engineering Note, "ES-7138 Quad Linear Fan-In," Fermilab Engineering Drawing # 089200-AC-46573, Oct. (1977).
6. LeCroy User's Manual for Camac Model 4300, 16 channel, Fast Encoding and Readout ADC (FERA), April (1984).
7. LeCroy User's Manual for NIM Model 127FL, Dual Bi-polar Linear Fan-In, June (1974).
8. A.P. Chikkatur *et al.*, NuTeV/CCFR Collabora-

tion, Z.Phys. **C74**, (1997).
9. P. S. Auchincloss *et al.*, CCFR collaboration, Nucl. Instrum. Meth. **A343**, (1994).
10. J. Krider, "Single Wire Drift Chamber Design," unpublished (1987).
11. T. Toohig, "Fermilab Magnets, Power Supplies, and Auxiliary Devices: Technical Data," Fermilab TM-632, December 5, 1975.
12. R. Juhala, "EPB Dipole Magnetic Field Measurements," Fermilab TM-434, July 26, 1973.
13. A. Alton, *et al.*, "Testbeam EPB Dipole Strength and Shape Parameterizations," NuTeV internal memorandum available at: http://www-e815.fnal.gov/~bolton/epb_bdl.ps.gz.
14. Photomultiplier Tubes, Hamamatsu Photonics K.K., Shimokanzo, Japan, 1988.
15. C.W. Fabjan and T. Ludlam, Ann. Rev. Nucl. Part. Sci. **32**, 335 (1982).
16. GEANT Detector Description and Simulation Tool, CERN Program Library Long Writeup W5013.
17. T.A. Gabriel and D.E. Groom, Nucl. Instr. Meth. **A338**, 336 (1994).
18. H. Fesefeldt, PITHA 85/02 (Aachen 1985).
19. A. Fasso, A. Ferrrari, J. Ranft and P. R. Sala, Proc. IV INT. Conf. on Calorimetry in High Energy Physics, La Biodola (Is. d'Elba),Sep. 20 - 25, 1993 ed. A. Menzione and A. Scribano, World Scientific, p 493.
20. C. Zeitnitz and T.A. Gabriel, Nucl. Instr. Meth. **A349**, 106 (1994).
21. A. Ferrari and P.R. Sala, ATLAS Internal Note PHYS-No-086, June 1996.
22. R. Wigmans, Nucl. Instr. Meth. **A259** 389(1987); R. Wigmans, Nucl. Instr. Meth. **A265** 273 (1988).
23. J. Liu (CDF collaboration), Fermilab-conf-97-414-E, Aug. 1997, to be published in Proceedings of the 7th International Conference on Calorimetry in High Energy Physics (CALOR 97), Tuscon, AZ, Nov. 1997.
24. S. Avvakumov *et al.*, NuTeV collaboration, UR-1562 (Jan. 1999), in Proceedings of the 6th International Conference on Advanced Technology and Particle Physics, Villa Olmo, Italy, October 1998.